**UNIVERSITY OF
OSLO**
Department of Physics

Total Pressure Wavefield Computation for Rough Sea-Surfaces

Master Thesis
in Electronic

Parisa Ghasemi

August 2014

Acknowledgement

I would like to express my special gratitude and appreciation to my supervisors Associate Prof. Andreas Austeng at the Department for Informatics (Ifi), University of Oslo, and Dr. Walter Söllner, Dr.Okwudili C. Orji and Dr. Endrias G. Asgedom at PGS for their invaluable contributions and good advices throughout this thesis.

Furthermore, I would like to acknowledge my deepest gratitude to PGS and all those who provided me the possibility to complete this thesis.

A special thanks to my family. Words cannot express how grateful I am to my beloved husband and lovely daughter for their patience and all of the sacrifices and supports that they made on my behalf. At the end, my gratitude goes to my mother and father for their prayer for me, which was what, sustained me thus far.

Parisa Ghasemi

Oslo, 25rd August 2014

II

Abstract

Marine seismic data acquisition with dual-sensor streamers (Geostreamer) enables separating the total wavefield in its up-going and down-going pressure and velocity components. The separation step is largely independent of the subsurface model and sea-surface shape. As a consequence realistic rough sea-surface shapes need to be included also in modelling studies and survey design. However, modelling of seismic data with rough sea-surface is not trivial and most of the standard modelling tools are still limited to flat or smoothly varying sea-surfaces. The scope of this thesis is to investigate including realistically rough sea-surfaces in PGS' modelling software Nucleus+. From Rayleigh's reciprocity theorem in acoustic media, an integral expression for computing the down-going pressure wavefield from the up-going velocity wavefield and the sea-surface reflectivity is derived. The sea-surface reflectivity is computed based on Helmholtz-Kirchhoff integral using a free-surface boundary condition (Orji et al., 2011) and the up-going vertical particle velocity wavefield is computed as subsurface modelling from Nucleus+. The computation accuracy of the derived down-going pressure wavefield depends mainly on the numerical solution of the integrals and is proved by comparing with the total pressure field from Nucleus+ using smooth and flat sea-surfaces. Edge effects in the calculated down-going pressure wavefield are partly suppressed by using a cosine tapered window. Finally, the modelling is tested on a realistically rough sea-surface derived from a Pierson-Moskowitz (PM) spectrum. The total pressure field is computed by adding the computed down-going pressure wavefield including the effects of the realistic sea-surface to the modelled up-going pressure wavefield from Nucleus+.

IV

Table of Contents

Chapter 1

Introduction

Seismic survey is a well-known technique in geophysical prospecting among the various remote sensing methods that can be used to measure the earth physical properties and evaluate subterranean formations to search for hydrocarbon accumulation. In marine seismic survey, seismic energy sources, airguns or marine vibrators are used to generate the seismic signal. The generated seismic wave travel downward through the water to the sea floor. In the sea bottom there are different layers with various elastic properties, which lead to different acoustic impedance at the interfaces. The seismic energy is reflected partially from this interfaces which act like reflectors. The reflected seismic signal is detected by seismic sensors, hydrophones or geophones, at the sea-surface or at a desired depth from the surface in boreholes.

Seismic data are processed employing various methods of signal processing which are fundamentally based on wave theory in order to extract as much information as possible about the subterranean formation. The processed seismic images representing slices through the geological model are input to workstations where the actual interpretation, to locate oil/gas accumulation, takes place. Interpreting seismic images partly depends on the interpreter's skills/knowledge of the area and partly on the quality of the processed seismic image. If the resolution of the seismic image is poor the interpreter will not be able to locate any oil/gas accumulation. Thus, the chief objective of seismic data processing is to achieve high resolution or in other words high signal-to-noise ratio.

The sea-surface is a perfect reflector generating source and receiver ghosts (Ghosh, 2000). In marine seismic data acquisition, the sea-surface reflections (ghosts) introduce periodic notches in the spectra of seismic data that reduce data resolution. Ghost reflections in addition to multiples may cause misinterpretation of the recorded data if not removed or attenuated accurately. The effects of rough sea-surface ghosts are much more than that of flat sea-surface. Methods of mitigating the effects of sea-surface ghost using the sea-

surface profile information have been recently developed (Amundsen, 2005). Data recorded by dual sensor streamers comprising pressure and vertical particle velocity sensors can be employed in separating the recorded data into the up-going and down-going pressure or the corresponding velocity wavefields, which eliminates the receiver side ghost implicitly. Consequently using dual sensor streamer can improve the seismic images resolution.

A crucial step before performing a seismic survey is modelling. This is required to optimize the acquisition parameters. The modelling algorithms for survey design have been developed in PGS since the first efforts of source modelling by Ziolkowski (1970) up to now, leading to sophisticated algorithms and advanced integrated package of seismic tools. Seismic modelling helps better understanding how seismic waves generated by single airguns (or airgun arrays) in marine environment propagate through different media and layers in the subsurface. The seismic modelling tools can be used to determine design parameters (such as source and receiver locations or array spacing), predict the results and achieve an overview of the survey. Moreover the feasibility of the survey can be tested by modelling. A good understanding of various types of seismic sources (typically array of airguns in marine seismic data acquisition) and recording systems that may contains streamers of hydrophones and geophones, is necessary to enhance the accuracy of seismic acquisition. There are many types of seismic modelling techniques and some limiting factors related to each type of modelling, such as accuracy, time consuming, and economic constraints that should be considered. Among the many types of modelling methods the two most important are, ray tracing and full wavefield methods based on finite-difference schemes.

The ray tracing method may be separated into kinematic ray tracing and dynamic ray tracing. First a 2D or 3D layered model is constructed. By using differential equations over a continuous block of model the ray path and travel time along that ray are calculated by kinematic ray tracing. In dynamic ray tracing a system of differential equations is used to calculate the dynamic content along the ray path (amplitude coefficients, wavefront curvatures). By modelling based on ray tracing method, it is possible to record all the geometric dimensions of a ray comprising dynamic parameters.

The finite difference (FD) method is used to simulate propagation of seismic wave in more complex models. In this method, a gridded model of earth is considered with certain elastic properties characterized by P and S wave velocity, density and absorption. The spatial and temporal derivatives in the wave equation at each grid position are approximated by finite differencing. The computation time and cost of this method is high. This method is used for models with complex geology.

The PGS proprietary software Nucleus is state-of-the-art software for seismic modelling and survey designing. It comprises a suite of tools that can be used to design various types of seismic survey scenarios including those using streamers, ocean bottom cable (OBC), ocean bottom nodes, marine electromagnetic sensors etc. Nucleus modelling methods include ray tracing and finite difference. As an example for using Nucleus+, the users have the possibility to define different parameters such as vessel parameters (recording length, number of sources and streamers, source and streamer depth, group interval, position of sources and first receiver on streamer and …) and actions (defining the model, number of interfaces and diffractors, V_P and ρ for each layer, defining the type and direction of streamer survey) during modelling and save it as a job which is accessible for later editing.

In marine survey modelling using Nucleus+, the sea-surface is considered flat and stationary. The main goal of this thesis is to include realistic sea-surface into the PGS proprietary software (Nucleus+) in order to make the data modelling more realistic . The ray-tracing based modelling will be extended using an integral relationship to include the ghost reflection generated by rough sea-surfaces. The down-going pressure wavefield (ghost) will be computed from the up-going vertical particle velocity wavefield and the rough free-surface reflectivity (or Green's function). Furthermore, we compute the total wavefield by adding the calculated down-going wavefield to up-going wavefield from Nucleus+. Finally, this will be validated by comparing the total wavefield obtained based on this technique and that obtained from Nucleus+ for a flat sea-surface case.

The following problems are addressed in this thesis:

I.   Modelling the sea-surface reflection from flat, sinusoid, Pierson-Moscowitz spectra based rough sea.
II. Computing the down-going wavefield by first determining the sea-surface reflectivity based on Helmholtz-Kirchhoff integral technique (Orji et al., 2011) and combining this with up-going vertical particle velocity wavefield computed from any forward modelling software (e.g. Nucleus+).

1.1 Thesis Structure

Chapter 2

This chapter provides an introduction to geophysical prospecting with seismic waves. The main problem with marine seismic data acquisition (e.g. the ghost reflection from the sea-surface) will be described. It also introduces various marine towed streamer methods to attenuate the ghost with special focus on two-component streamer.

Chapter 3

This chapter describes sea-surface characteristics for flat and rough sea-surface (i.e. sinusoid and Pierson-Moskowitz spectrum based) and their wavefield scattering behavior. It also discusses challenges for modelling rough sea-surface based on ray-tracing or finite difference method. A physical model for a spatio-temporally varying sea-surface is described based on Pierson-Moskowitz spectrum and the corresponding reflectivity function is computed using the Kirchhoff-Helmholtz integral.

Chapter 4

In this chapter an integral relationship based on Rayleigh's reciprocity theorem is derived to compute the down-going wavefield reflected from the sea-surface. The down-going wavefield computation is considered for two cases: (i) when sources are above the receivers and (ii) when sources are below the receivers.

Chapter 5

This chapter describes the generation of synthetic data for a marine seismic survey with dual-sensor streamer. After defining the controlled sub-surface model, the sea-surface response is modeled using Kirchhoff-Helmholtz integral. Finally, the down-going wavefield is constructed for the given sea-surface state. This chapter also provides a discussion regarding the computed down-going wavefield data.

Chapter 6

This chapter summarizes the work and presents the conclusion associated with the main goal of the thesis and the problems that has been solved. It also gives some suggestion for future work.

Chapter 2

Background

2.1 Introduction

This section gives an overview of the fundamental principles of geophysics. Moreover this chapter provides a background of marine seismic survey and related terms for modelling to have a better understanding of the objectives.

2.2 Seismic Survey

In a geophysical survey, different techniques are used to collect geophysical data for field studies. These data maybe collected from over or under the earth or from areal, orbital or marine platforms. Geoscience, marine science, archaeology and energy exploration are some of geophysical survey applications.

Remote sensing is used for the acquisition of information when there is no direct physical access to measure the phenomenon of interest. It is splitted into active remote sensing when the energy source is provided to illuminate the object or area of the interest or passive remote sensing which measure the reflected energy when the natural energy source is available (earthquake, sun, etc.).

The formation and features of the earth interior in a target area is sensed remotely by the geophysical survey equipment. The presence of hidden resources within the subsurface can be measured by geophysical surveying.

Seismic survey is a form of geophysical survey to measure the earth physical properties such as magnetic, electric, thermal, gravitation and elastic. It is performed to understand the structure and formation of the subsurface mostly for gas and oil exploration. Different methods of seismic data acquisition are

used to determine the probability of petroleum resources existent in an area. In a seismic survey, seismic sources generate seismic waves that travel through various media such as water, sediment layers or rock layers. Different kind of seismic sources can be used to generate seismic energy. Chemical explosive sources are more popular for onshore surveys, vibrators for hydrocarbon exploration or air gun for marine seismic surveys. Seismic receivers (receiver arrays) such as geophones or hydrophones record the waves that are reflected or refracted by the seismic reflectors. The receivers (sensors) detect the seismic signals from the back scattered energy used for further processing. The seismic data is processed to extract information about the geological structure and properties of the earth subsurface formations of the surveying area.

According to the propagation properties main types of seismic waves are: direct, reflected, refracted and surface waves. By utilizing each type of seismic waves there are three main types of seismic survey: reflection, refraction and surface waves. Figure 2.1 shows a seismic source and main seismic waves according to the propagation properties.
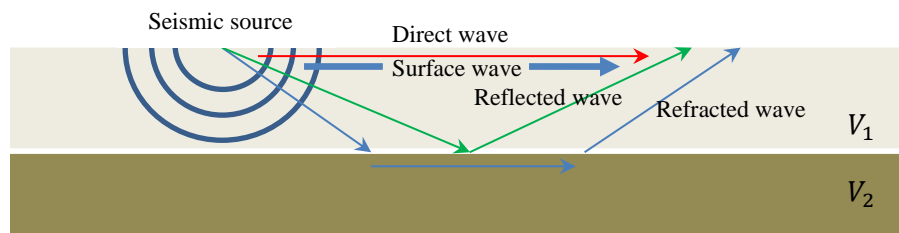

Figure 2.1: Main seismic waves according to the propagation property.

- **Reflected wave,** when a wavefront at an interface between two different media changes its direction and returns to the medium of origin. There are two types of reflection: specular reflection from a very smooth interface, when the angle made by the incident ray and reflected ray with normal are equal, and diffuse reflection when the surface is rough and rays bounces off in all directions.

- **Refracted wave,** when a wave travels from a medium to another medium and its direction changes. By changing the medium the phase velocity ($v_P = \frac{\lambda}{T}$) of a wave is changed but the wave's frequency remains constant. The relation between the refraction and incident angles is described by Snell's law:

$$\frac{sin\,\theta_1}{sin\,\theta_2} = \frac{v_1}{v_2} = \frac{n_2}{n_1}$$
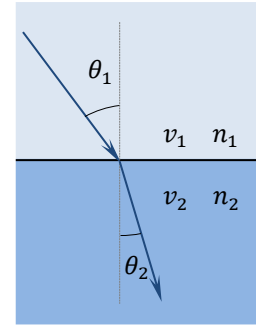
Figure 2.2: Refraction of an incident ray at interface between two media with different refractive indices $n_2 > n_1$. The phase velocity is higher in the upper medium $v_2 < v_1$. The refraction angle is less than incidence angle $\theta_1 > \theta_2$.

- **Direct wave,** is a type of seismic wave, which travel direct from the source to the receiver without being reflected or refracted from a seismic reflector.

2.3 Marine Seismic Data Acquisition

Marine seismic survey is an offshore geophysical exploration. For offshore seismic data acquisition, large seismic vessels are used. The vessels deploy one or several air gun arrays as sources that force highly compressed air into water for generating seismic signal. The receiver cable that is towed by the vessel is called streamer. The streamers comprise groups of hydrophone (made for example by piezoelectric material) at specific intervals, which are sensitive to pressure changes. Marine seismic data can be collected by a single streamer along a line of receivers (in 2-D acquisition) or several (up to about 20) long streamers at the same time (in 3-D acquisition). Imaging by seismic data from 3-D seismic survey is more accurate than from 2-D because it utilizes multiple points of observations.

One of the main problems in marine seismic data acquisition is ghost effect. The sea-surface (air-water interface) acts like an acoustic mirror (Ghosh, 2000), which causes ghost effects in recorded seismic data. The seismic waves that travel upward to the air-water interface will reflect off the sea-surface. The reflected wave from sea-surface is known as marine seismic ghost, which is an undesirable wave in marine seismic data acquisition. The ghost effect exists at both the source side and receiver side of any towed streamer. The ghost rays continuously interfere with the primaries through the recording length of each shot record. The nature of interference between the ghost wavefield and the primary wavefield depends on the source depth for source ghost and depth of the streamer for receiver ghost.

As it is seen in Figure 2.3 from source to receiver four different rays can be produced: direct ray, ghosted only at the source side, ghosted only at receiver side, ghosted at both source and receiver sides.
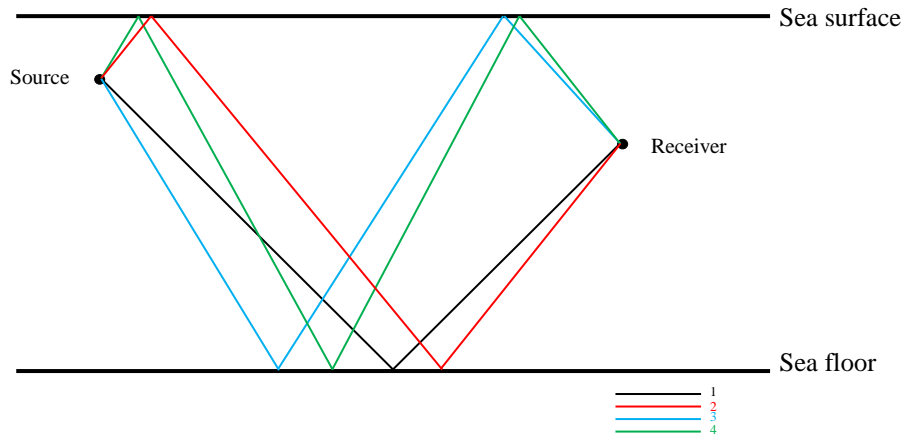
Figure 2.3: Event "1" is the primary ray path taken from source array to target to receiver. Event "2" shows the source ghost reflected ray from the sea-surface, event "3" shows the ghost reflection from sea-surface at receiver side event "4" comprises both a source ghost and a receiver ghost reflection. The ghost reflections interfere with the primaries and decrease the resolution of the seismic images so all events 2, 3 and 4 are unwanted.

The source and receiver ghost nature and ghost function will be discussed in details later in the following subsections.

2.4 The Source and Receiver Ghost

As mentioned previously, the sea-surface is a perfect reflector. Some of the energy generated by the marine seismic source goes upwards where they are reflected at the air-water interface. This reflected wave is known as the source ghost.
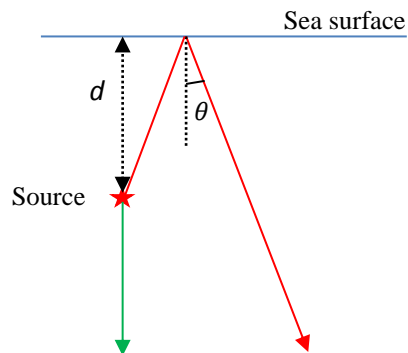

Figure 2.4: A sketch of source ghost, the direct wave is shown by the green color and the reflected energy from sea-surface (ghost) by red color.

The time-delayed reflected wavefield follows the seismic wavefield that travels direct from the source to the sea bottom and affect both the low and high frequency information. By considering the vertical travel path, the emitted energy from the source and its ghost will sum destructively (sum to zero) at harmonics of the frequency $f = v/2d$ ($v = \frac{2d}{t}$, $t = \frac{1}{f}$) where v is the water velocity and $d = \frac{v}{2f}$ is the depth of the source. The source wavefield and ghost wavefield will sum constructively at harmonics of frequency $f = v/4d$. The peaks and notches that can be seen in the amplitude spectrum of the seismic data in Figure 2.7 are as a result of the constructive and destructive summation process. Consequently, some of the information will be missed and the area of interest cannot be fully imaged.

In the case of non-vertical travel paths, the time delay between the original wavefield and the ghost wavefield will be angle dependent, that is leading to the change of frequencies with takeoff angle of energy from the source where the destructive or constructive summation take place.

The amount of the energy being reflected from the sea-surface depends on the condition of the sea-surface, which is rough or flat, since a rough sea has a lower reflection coefficient than a calm one.

Reflection coefficient

When there is discontinuity in wave propagation path in a medium and the seismic wave strikes an interface between two medium with different seismic impedance, reflection coefficient is utilized. Reflection coefficient is computed by using acoustic (seismic) impedance contrast between the two medium. Acoustic impedance is defined by equation below:

$$Z_0 = \rho v$$

where ρ is density and v is the seismic wave velocity.

Reflection coefficient at normal incidence is defined by equation:

$$R = \frac{Z_1 - Z_0}{Z_1 + Z_0}$$

where Z_0 and Z_1 are the impedance of the first and second medium, respectively.

Reflection coefficient at air-water interface**:**

Impedance for air $Z_1 = 415 \; \Omega$ and

Seawater impedance $Z_0 = 1.54 \times 10^6 \; \Omega$

Reflection coefficient

$$R = \frac{Z_1 - Z_0}{Z_1 + Z_0} \approx -1$$

The sea-surface is a perfect reflector with a reflection coefficient of -1 or phase shift of 180 degree.

If $s_0(t)$ denotes the direct source pulse from the airgun array so the combined pulse can be:

$$s(t) = s_0(t) - s_0(t - \tau)$$

$$\tau = \frac{2d}{c_0}$$

where τ is the time delay, d is the source depth and c_0 is the sound speed in water. The angle θ is considered zero here (GeoClass, Seismic Acquisition, 2.5 The source ghost).

The ghosting effect also can be seen on the receiver side (see Figure 2.5). The up-going wavefield which contains the original source wavefield and its ghost alongside arrive at the receivers and continue traveling upward to the sea-surface where being reflected downward with the reverse polarity. The reflected wavefield and the up-going wavefield are recorded by the receivers simultaneously. Therefore, at receiver side a time delayed reflected wavefield from the sea-surface interferes with the seismic wavefield directly scattered from the sea bottom to the receiver. The summation of the up-going and down-going wavefield at the receivers creates a second set of notches in the amplitude spectrum of the data, which increases some frequencies and decreases the others (Baldock et al., 2013).

The receiver ghost can be modeled in the same way as the source ghost. For vertical incident the depth of the streamer can be estimated from the equation:

$$D = \frac{\pi c_0}{\omega_1} = \frac{c_0}{2f_1}$$

where c_0 is the sound speed in the water and f_1 is the frequency of the first notch in the receiver ghost filter (GeoClass, Seismic Acquisition, 3.4 Receiver ghost).
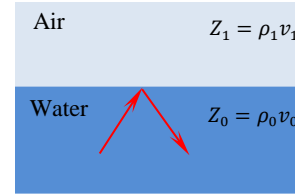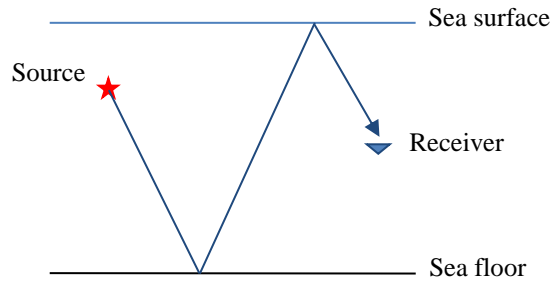
Figure 2.5: A sketch of the receiver ghost.

In the case of non-vertical travel path, like the source ghost the receiver ghost is angle-dependent (Baldock et al., 2013). Figure 2.6 shows clearly that in the case of non-vertical incidence the source and receiver ghosts are angle dependent.
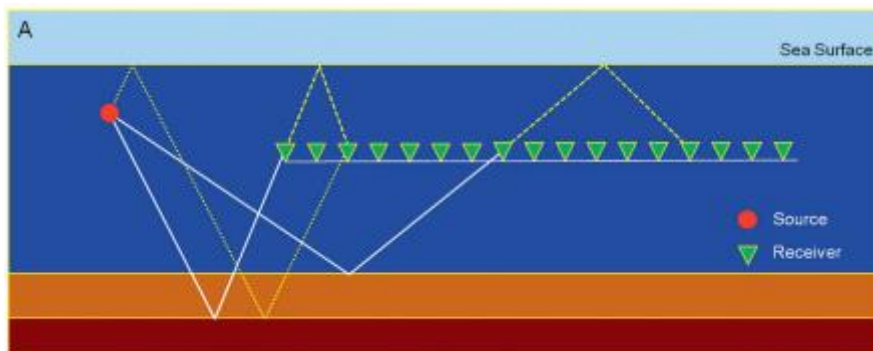

Figure 2.6: Diagram illustrates the angle-dependency of source and receiver ghosts (Picture from: (Baldock et al., 2013)).

2.5 The Ghost Function

By getting Fourier transform of the combined and direct pulse, we can define the ghost filter:

$$G(\omega) \equiv \frac{S(\omega)}{S_0(\omega)}$$

The amplitude spectrum of the ghost filter is:

11

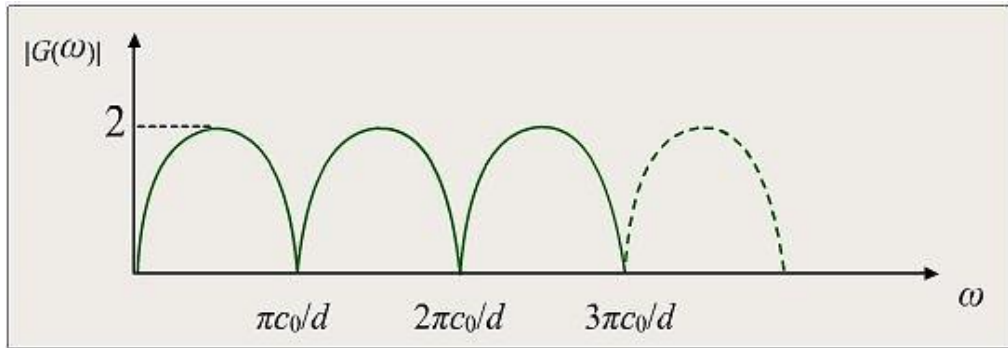$$|G(\omega)| = 2\left|\sin\left(\omega d / c_0\right)\right|$$

Figure 2.7: A sketch of the amplitude spectrum of the ghost filters (picture from GeoClass, Seismic Acquisition, 2.5.1 The ghost filter).

As we can see in the Figure 2.7 notches are at:

$$\omega_k = \frac{k\pi c_0}{d} \quad , \quad k = 0,1,2,\dots$$

The operational seismic data band width is considered between the first and second zeroes in the amplitude spectrum (GeoClass, Seismic Acquisition, 2.5.1 The ghost filter).

Different kind of streamer has been used to decrease the ghost effect and increase the bandwidth of the seismic data and resolution of the seismic images. The summary of some of these methods will be discussed briefly.

2.6 Marine Towed-Streamer Methods and Deghosting

Figure 2.8: A vessel with a towed source and streamers (Picture from GeoClass, Seismic Acquisition).

For marine seismic data acquisition the receiver cables (streamers) that comprise the hydrophones are towed by the large ships. As mentioned in details previously the ghost effect exists both on source and receiver sides. The ghost reflection from the sea-surface interferes constructively or destructively with primary reflections, which reduces the seismic bandwidth at the low and high ends of the spectrum (Moldoveanu et al., 2012).

The main problem in marine seismic data acquisition is the ghost effects. Different types of the solution that are proposed up to now are listed as follows.

- Slant streamer (Ray, 1982)
  The slant streamer contains the variable receiver depth along the streamer which leads to variable ghost from receiver to receiver to use in the stacking process. Deghosting solution for slant streamer relies on ghost notch variability from receiver to receiver. (Moldoveanu et al., 2012).

- Over/under streamers (Sonneland et al., 1986)

  In this method, two streamers are deployed by the ship on top of each other at large depths. The effect of swell noise can be minimized by this method. The recorded wavefileds by the over and under streamer at depth $d1$ and $d2$ respectively are written as a sum of up-going (U) and down-going (D) wavefields:

$$S1 = D1 + U1 , \qquad S2 = D2 + U2$$

  Limited utilization of this type of streamer was due to lack of streamer control in vertical and horizontal planes and the receiver position along the streamers.

- Hydrophone-vertical geophone streamers (Carlson et al., 2007)

  In this system the seismic pressure wavefield are recorded by the hydrophones and the vertical component of the particle velocity by the velocity sensors (Berni, 1985). Therefore by using this streamer, two different measurements can be combined to perform wavefield separation of up-going and down-going component of pressure wavefield. As a consequence the bandwidth of the seismic data is increased due to removing the receiver ghosts and low frequencies are improved by deploying deeper streamers (Semb et al., 2010). The dual-sensor streamer was introduced in 2007 which comprises hydrophones to measure the pressure wavefield and simultaneously geophones to measure the vertical component of the particle velocity (Carlson et al., 2007).

- Multicomponent (4c) towed-streamers (Robertsson et al., 2008)

  In this system the pressure is measured with hydrophones and particle acceleration with micro electromechanically systems (MEMS) in x, y and z directions. By using this system the temporal and the spatial bandwidth would be improved. Based on this measurements in addition to wavefield separation of up-going and down-going components, cross line wavefield reconstruction can be performed (Ozbek et al., 2010). Multicomponent streamers can be deployed at larger depths to decrease swell noise which improves low frequencies content, signal to noise ratio and acquisition efficiency (Moldoveanu et al., 2012).

The dual sensor streamer has been used in this work so it will be explained in more details in next section.

2.6.1 Dual-Sensor Streamer (Geostreamer)

The hydrophones that are used in the conventional streamers cannot distinguish between the opposite polarity of the up-going wavefield scattered from the sea floor and the down-going wavefield reflected from the sea-surface (the receiver Ghost). The down-going wavefield is the ghost reflection and the up-going wavefield is the seismic data without the receiver ghost. So as it is described in the ghost section, the summation of the up-going and down-going wavefields by the receiver will increase frequencies and reduce some others that causes reduced seismic image resolution and efficiency of seismic data collected by conventional streamer.

Geophones can detect the down-going wavefield with different polarity to the up-going wavefield. The dual-sensor streamer (Geostreamer) consists of collocated dual sensors; hydrophones and geophones (particle velocity sensors). It has been developed by PGS based on the wavefield separation principle. By using a dual-sensor streamer the pressure field is measured by hydrophones and simultaneously the vertical component of the particle velocity field is measured by geophones. The combined seismic wavefield from dual sensor recordings can be decomposed into the up and down-going pressure wavefield as well as the up and down-going vertical velocity wavefield.

Figure 2.9 show that the velocity sensor (geophone) records the same polarity for the up-going and down-going signals while the hydrophone records opposite polarity for up-going and down-going signals.

In a marine seismic survey, the seismic signal which is generated by seismic energy sources travel downward to the sea floor through a body of water overlying the subsurface of the earth, where it is partially reflected from the seismic reflectors (sea floor). The reflected signals are usually detected by seismic sensors (e.g., hydrophones) towed at a given depth in the water body before continue traveling upward where being reflected from the sea-surface and being recorded again by the sensors. The sea-surface usually acts like a mirror (Ghosh, 2000) and thus for a special case where it is assumed to be flat, the difference between the up-going wavefields and down-going wavefields is a phase shift of 180 degrees. Therefore, the total pressure P is given as:

$$P = U + D \,,$$

where U is the up-going wavefield and D is the down-going wavefield. Total vertical velocity is given as:

$$V_z = U^{(V_z)} + D^{(V_z)} \,,$$

where $U^{(V_z)}$ is the up-going component of the particle velocity and $D^{(V_z)}$ is the down-going component of the particle velocity.
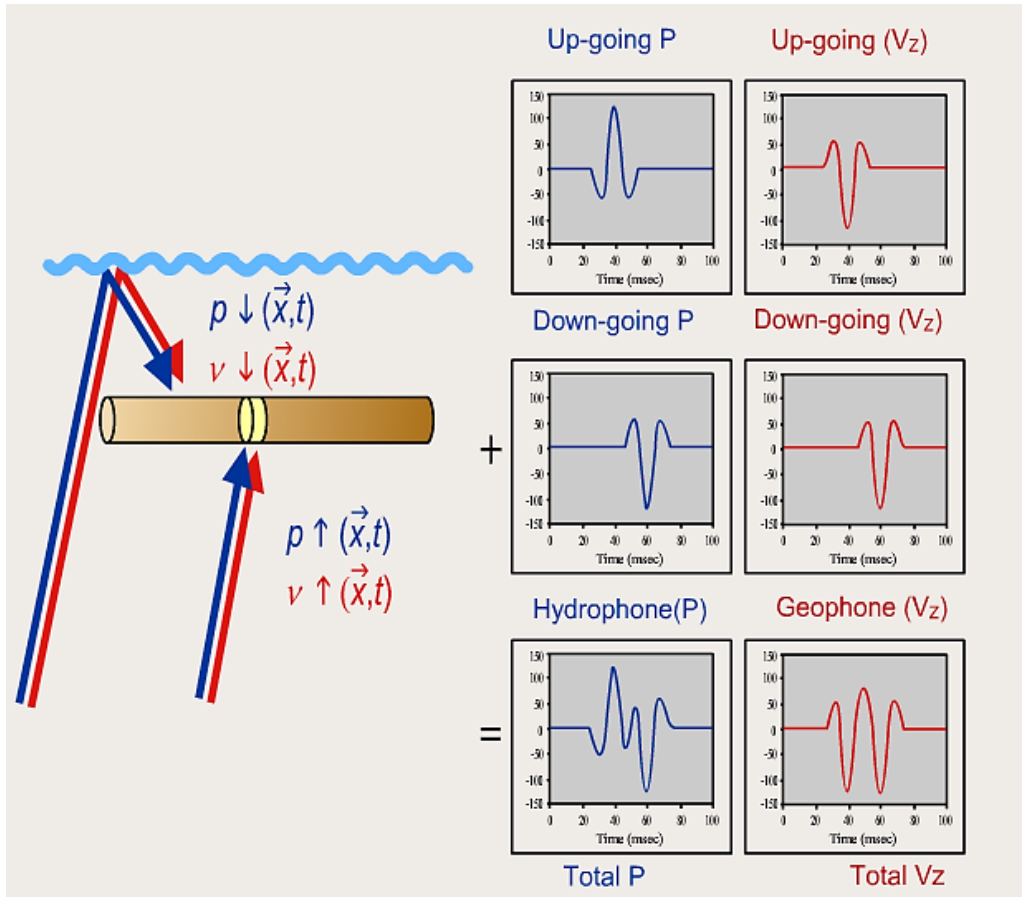
Figure 2.9: Schematic of the amplitude measurements of the up and down-going pulses and total wavefields by Hydrophone and Geophone (Picture from GeoClass, Seismic Acquisition, 3.3 Dual-sensor streamer (PGS)).

Relationship between pressure and particle velocity:

The relation between the particle velocity V_z and the pressure can be written as

$$V_z = \frac{-dp}{i\rho\omega dz} = \frac{k_z}{\rho\omega}(D - U), \quad i\omega \leftrightarrow \frac{d}{dt}$$

where ρ represents the density, ω is the angular frequency and k_z is the vertical wavenumber. The wavenumber can also be written as $k_z = \omega \cos\theta / c$ where c is the water velocity and θ is the angle of incidence (relative to the vertical).

The up-going U and down-going D wave constituent can be calculated from P and V_z such that their sum gives the total pressure field P,

adding P and V_z gives:

$$U = \frac{1}{2}\left(P - \frac{\rho\omega}{k_z}V_z\right),$$

GeoStreamer GS is the evolved form of the Geostreamer that presented by PGS. GeoStreamer GS is free of all source and receiver ghost. The ghost free seismic data can be acquired by utilizing both GeoSource (ghost free source) and Geostreamer (ghost free receiver). This technology provides a better data acquisition and in consequence better resolution of the seismic images (Towed Streamer Seismic, GeoStreamer GS, PGS Geophysical AS.).
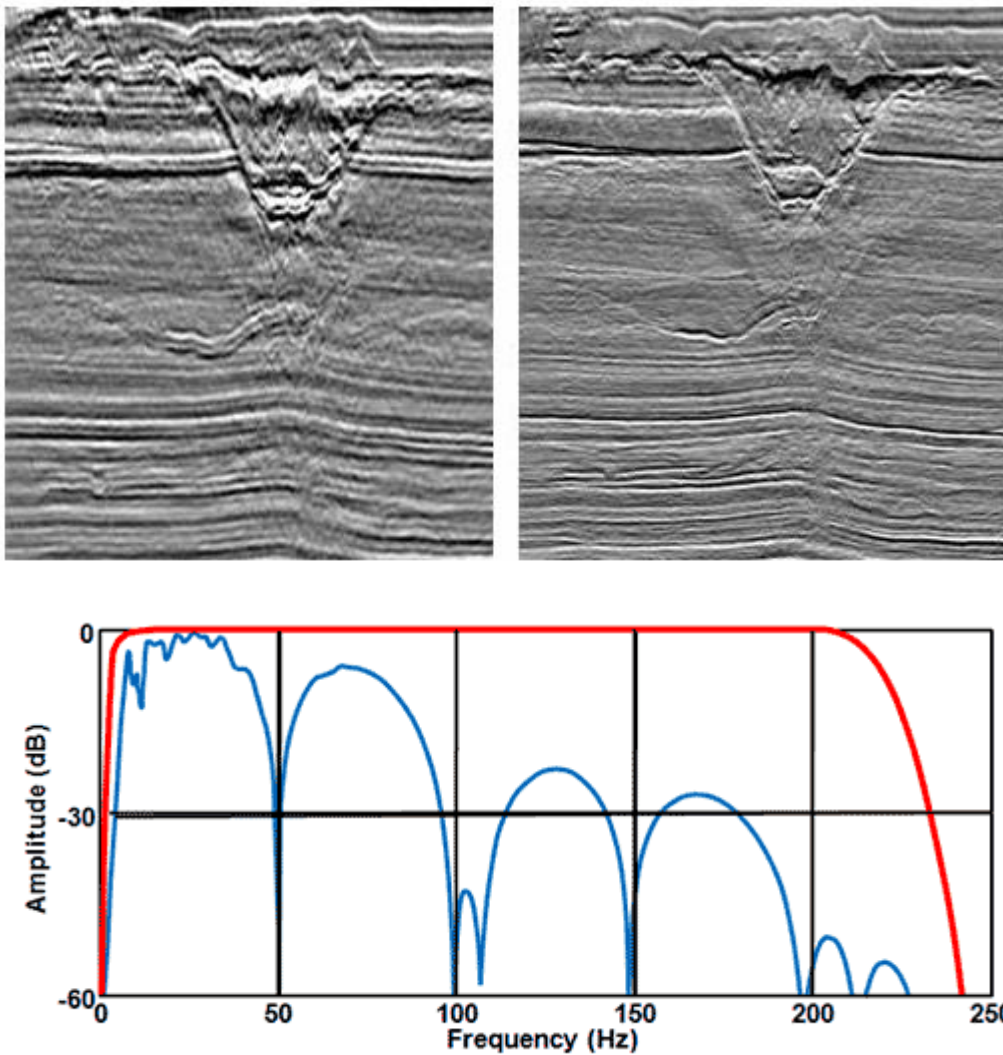

Figure 2.9: The seismic image on the left which is from conventional (hydrophone-only) streamer is contaminated with effects of the source and receiver ghost and displays significant loss of frequency content (blue spectrum), but the right seismic image from Geostreamer GS is entirely ghost-free and shows excellent resolution which is recovered signal frequencies in excess of 200 HZ (red spectrum) (Picture from Towed Streamer Seismic, GeoStreamer GS, PGS Geophysical AS.).

Figure 2.9 shows the ghost effects on a seismic image from a conventional streamer on the left with its amplitude spectrum (Blue spectrum) and ghost free image on the right from Geostreamer GS with a prominent resolution. Geostreamer GS recovers frequency more than 200 HZ that can be seen with red color in the amplitude spectrum.

Chapter 3

Reflectivity of a Rough Sea-Surface

In this chapter, basic characteristics of realistic rough sea-surfaces, their wave field scattering behavior and how to model these effects are discussed. A physical model for a spatio-temporally varying sea-surface is described based on Pierson-Moskowitz spectrum and the corresponding reflectivity function is computed using the Kirchhoff-Helmholtz integral.

3.1 Sea-Surface Characteristics

Flat Sea-Surface

A flat sea-surface cannot exist in nature. However, in modelling, flat sea-surface comprises of a layer with absolutely no fluctuation or variation in depth level. The scattering behavior of this type of surface is similar to a mirror, where the entire incoming waves scatter coherently in the specular direction (cf. Figure 3.1). Consequently, the reflection at the water–air interface can be described by Snell's law and the reflection coefficient can be obtained from plane wave solution of the wave equation (see Chapter 2). Thus, utilizing this assumption for processing and analyzing seismic data measured in the field may lead to miss-interpretation and miss-location of events (Orji et al., 2011).
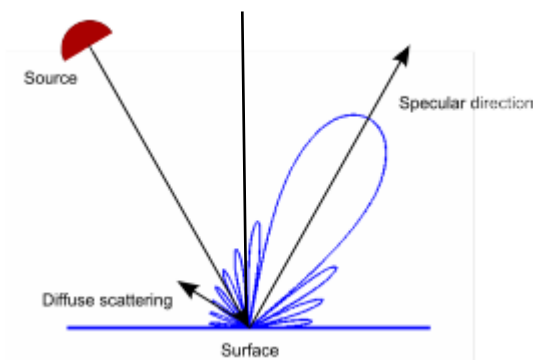
Figure 3.1: Illustration of the scattering from flat sea surface (Hansen, 2013).

Rough Sea-Surfaces

The roughness of a given surface can be characterized by its frequency spectrum and the wave height. For a wave incident on a rough surface, the vertical scale of roughness is given by the Rayleigh parameter:

$$P = 2k\sigma cos\theta$$

where k and θ are the incoming wave's wavenumber and angle of incidence, respectively. Moreover, σ is the root-mean-square height of the rough surface measured from the mean level and h (see Figure 3.2) is the surface height which is related to the root-mean-square height σ.

$$\sigma = (\langle h^2 \rangle)^{1/2}$$

When $P \ll 1$, the surface can be considered smooth and most of the incoming wave's energy scatters in the specular direction. However, when $P \gg 1$, the surface is significantly rough and most of the incoming wave's energy scatters incoherently. To explain the physical meaning of the Rayleigh parameter P consider a wave incident on a rough surface as shown in the Figure 3.3. If the surface is completely smooth, the two rays are specularly reflected, the reflected rays are in phase, and the reflection angle is equal to the incident angle θ. However, if the surface is rough, the two rays are not in phase. The phase difference is given by $2k\sigma cos\theta$. Thus, Rayleigh's paramter P is a statistical measure of phase difference.

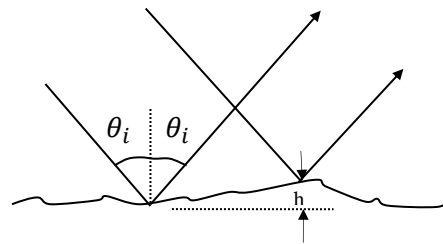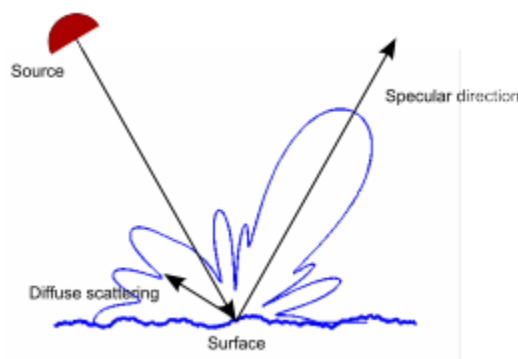**Figure 3.2**: Rayleigh criterion of surface roughness.

Figure 3.3: Illustration of the specular reflection and diffuses scattering at rough surface (Hansen, 2013).

In the case moderately rough sea-surfaces, the incoming wave's energy scatter both coherently and incoherently (cf. Figure 3.3). Therefore, as the surface gets rougher, the scattered energy in the coherent direction gets smaller while the energy in the incoherent direction gets bigger (cf. Figure 3.4).
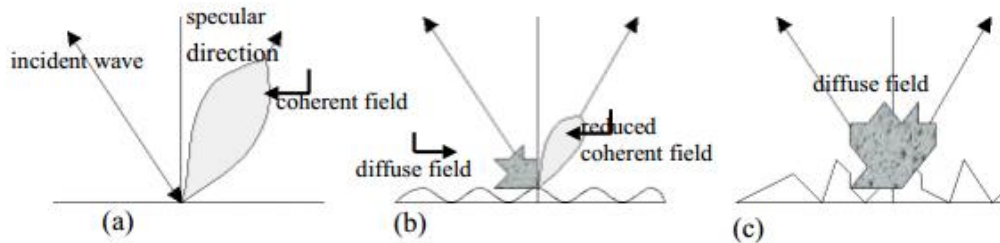

Figure 3.4: Comparison of the components of a backscattered wave according to the rate of roughness from (a) smooth, (b) rough (sinusoidal), (c) very rough surface. Picture from (Hajnsek et al., 2005)

Rough Sea-Surface based on Pierson Moscowitz spectrum

Wavy shape of the sea-surface, in reality, is formed by different kinds of perturbations that are natural (e.g. earthquake, gravity and wind) or artificial (e.g. ships). Our main interest in this section is to describe a physical model for the sea-surface variation as a result of wind. Wind is the dominant source of surface waves in sea. The sea condition can be predicted by using the wind wave models based on the sea wave's spectra. The waves are determined by the parameters such as wave height, wave period and power spectrum.

Pierson and Moskowitz represented an empirical wind wave model in 1964. According to this model the spatial spectrum is defined from the wind speed and the spatial wavenumber. Pierson and Moskowitz assumed that if the wind blows over a large fetch, finally the wind and the wave generated by the wind over the sea-surface reach a balance point. This state is known as developed sea. Assume the wind blow over the smooth calm sea. Small waves are generated because of the pressure changes at the sea-surface caused by the turbulence of the wind. Larger waves are produced by continued blowing of the wind over the small waves. The interaction between wind and the wave produces pressure differences that causes growing of the waves. This is an unstable process because the pressure differences are increased as the waves become larger that lead the growing of the waves to become faster. The unstable process in the growing of the waves causes those to grow

exponentially (Miles, 1957). The larger waves are produced by the interaction of the waves with each other (Hasselmann et al., 1973). As a consequence of this interaction the energy of the wave shifts from short waves to the waves with the frequencies slightly lower than the waves with the frequencies at the peak of the spectrum which increases the speed of the waves to go faster than the wind.

The power spectrum of the sea waves can be obtained by Pierson-Moskowitz equation:

$$W(K_j, K_l) = \left[\propto / \left(2|K_{jl}|^3 \right) \right] e^{-(\beta g^2)/(K_{jl}^2 U_w^4)}, \tag{3.1}$$

where K_j and K_l are x and y components of absolute wavenumber respectively

$$K_{jl} = \sqrt{K_j^2 + K_l^2},$$

U_W is the speed of the wind (measured at 19.5 m height),

$\propto = 8.10 \times 10^{-3}$ and $\beta = 0.74$ and g is the acceleration due to gravity.

The 1D Pierson-Moskowitz spatial roughness spectrum can be written as:

$$W(K) = \left[\frac{\alpha}{4|K|^3} \right] e^{-(\beta g^2)/(K^2 U_w^4)}, \tag{3.2}$$

where K is the wave (at sea-surface) spatial wavenumber and the other parameters are like Eq. (3.1) for 2D. The wave height at the sea-surface can be captured by taking random phase shifts between components of each wavenumber (Orji, 2012). The wave (sea-surface) height function at the running point $x^{'}$ (a point that can be anywhere on the sea-surface, see figure 3.5) is given as:

$$f(x^{'}) = \frac{1}{L} \sum_{j=0}^{N-1} F(K_j) e^{iK_j x^{'}}, \tag{3.3}$$

where $K_j = 2\pi j/L$ and L is the surface spatial wavelength.

for $j \geq 0$,

$$F(K_j) = [2\pi L W(K_j)]^{1/2} \begin{cases} N(0,1) + iN(0,1)/\sqrt{2}, j \neq 0, N/2 \\ N(0,1), j = 0, N/2 \end{cases} \tag{3.4}$$

and for $j < 0$,

$$F(K_j) = F(K_{-j}).$$ (3.5)

The random number $N(0,1)$ is generated by a Gaussian distribution with zero mean and unit variance. So, the sea-surface can be formed by getting summation over the wavenumber components after taking random phase shift between them.

For modelling the energy balance at the sea-surface the angular weight factor is considered $cos^2(\theta)$, where θ is the angular difference between the direction of the wind and the wavenumber components direction. Further empirical studies have shown that the angular distribution is not dependent only to the wavenumber but near the peak of the wavenumber (Komen, Hasselmann and Hasselmann, 1984). Due to the experimental evidence a directivity correction has developed by Hasselmann et al. (1980) for an isotropic sea-surface spectrum. For directivity correction a directional term will multiply with the power spectrum of the sea-surface from Eq. (3.1). Considering the separation of the propagated waves at the sea-surface due to their directions and wavelengths the deep water dispersion relation is applied (Orji, 2012).

The deep water dispersion relation is given by

$$\Omega_{jl} = \sqrt{gK_{jl}},$$

where Ω_{jl} is the spatial angular frequency.

The sea-surface variation can be generated by combining the directional Pierson-Moskowitz spectrum and the dispersion relation.

3.2 Modelling Seismic Data from a Rough Sea-Surface

The two widely used methods for modelling seismic wave propagation are ray tracing and finite difference. In this section, we briefly summarize the underlying principles of these two modelling methods and explain their drawbacks when it comes to modelling of seismic data from a rough sea-surface.

3.2.1 Modelling by Ray Tracing

Ray tracing approximates the wave equation in order to obtain the ray path, travel times and amplitude coefficients for a wave propagation problem in 2D or 3D media. Snell's law is used to trace the ray paths and Fermat's principle is

utilized to compute the travel times (i.e. kinematic ray tracing). Modelling by ray tracing is a high frequency approximation solution for the wave equation and hence requires that the variation of velocity in the medium under consideration should be smooth enough within one wavelength (Sun et al., 1997). However, rough sea-surface could be varying spatially more than the requirement of the ray tracing method and consequently results in an error.

3.2.2 Modelling by Finite Difference

The finite difference (FD) method is a robust numerical method applicable to model wave propagation in complex earth models. In the FD method, a computational domain is covered by a space-time grid. The spatial and temporal derivatives in the wave equation at each grid position are approximated by finite differencing. Model seismic wave propagation in a medium with rough sea-surface has two main disadvantages: first, in order to use FD we need to discretize the continuous sea-surface, however depending on how small the grid sizes are every grid point in the sea-surface acts like an artificial elementary diffractor. Second, realistic sea-surface varies both in space and time and these requires solving Navier-Stokes equations which is rather complex and computationally intense.

3.3 Sea-Surface Reflectivity Function

To derive the reflectivity of a given sea-surface variation, we start with the Kirchhoff-Helmholtz integral equation in the frequency domain (Orji et al., 2011):

$$
P(\vec{r}, \omega) = P_{inc}(\vec{r}, \omega)
$$
$$
- \frac{1}{4i} \int_{\partial l} \left[H_0^{(1)}(k|\vec{r}' - \vec{r}|) \right] \frac{\partial P(\vec{r}', \omega)}{\partial n'} d l' \ , \qquad (3.6)
$$

where the first term represents the direct wavefield and the second term the scattered wavefield from the sea-surface.

$$
P_{inc}(\vec{r}, \omega) = \frac{1}{4i} H_0^{(1)}(k|\vec{r}_d|) S(\omega) \ , \qquad (3.7)
$$

$H_0^{(1)}$ is the zeroth-order Hankel function of the first kind, $S(\omega)$ represents the source spectrum, k is the wavenumber of the propagating wavefield and $d l'$ is the length parameter along the rough surface. With reference to Figure 3.5:

$f(x)$ represent the surface height function; $\left[x', f(x') \right]$ defines the position of a scattering point on the surface; $\bar{r}'$ defines a vector from the origin to the running scattering point; $\bar{r}$ defines a vector from the origin to a fixed receiver position; $\bar{r}' - \bar{r}$ is a vector from a given receiver position to the running scattering point; $\bar{r}_d$ is a vector from a source position to the receiver; $\bar{r}_s$ defines a vector from origin to the source position.
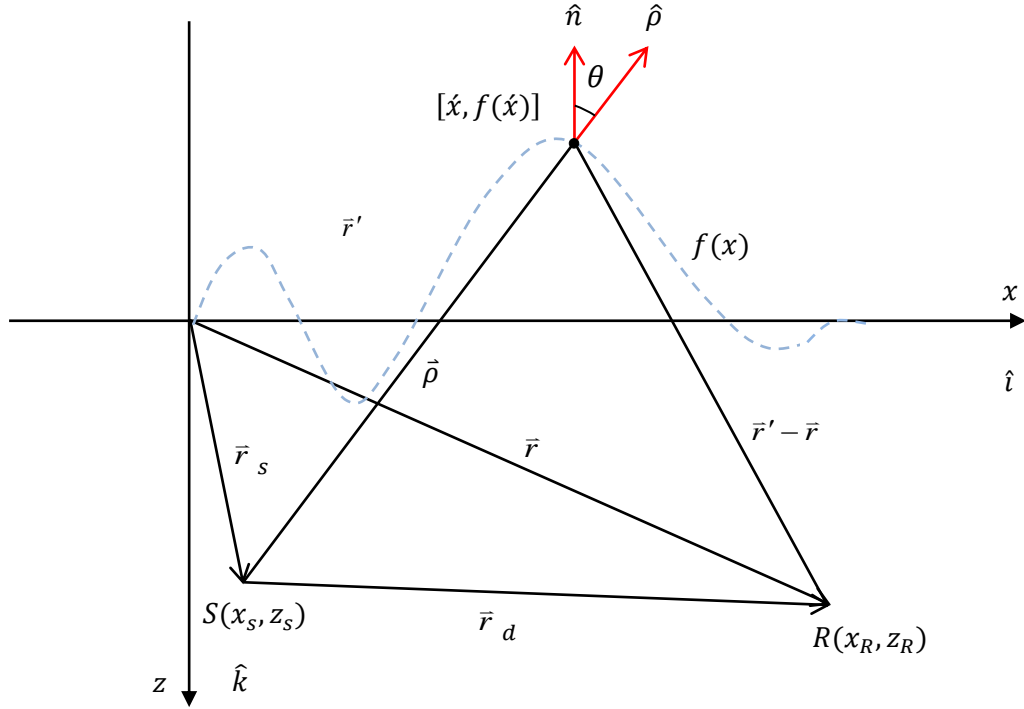
Figure 3.5: A sketch showing the coordinates of the source S, the receiver R, and the running scattering point $\left[x', f(x') \right]$ on the sea-surface $f(x)$ (Picture from (Orji et al., 2011)).

$\vec{\rho}$ defines the vector from the fixed source position to the running scattering point; the unit vectors $\hat{n}$ and $\hat{\rho}$ respectively denote the normal to the surface and the unit vector direction of the incident field at $\left[x', f(x') \right]$; the obliquity factor is given by

$$cos\ \theta = \hat{n} . \hat{\rho} \equiv \eta(x') \text{ (See Figure 3.5)}$$

When the surface is locally planar on the scale of the dominating acoustic wavelength, the Kirchhoff approximation can be used to approximate the pressure gradient:

$$\frac{\partial P(\vec{r}, \omega)}{\partial n} \cong \frac{2\partial P_{inc}(\vec{r}, \omega)}{\partial n} \quad , \quad\quad\quad (3.8)$$

Finally, the frequency-domain Kirchhoff-Helmholtz integral can be written as: (in our case we need just the second part of the equation which is the scattered wavefield from the sea-surface)

$$P_s(\vec{r}, \omega)$$
$$= \frac{kS(\omega)}{8} \int_{\partial L} H_0^{(1)} (k|\vec{r}' - \vec{r}|) H_1^{(1)} (k|\bar{\rho}|) \eta(x') dx', \quad\quad\quad (3.9)$$

where $H_0^{(1)}$ is the zeroth-order Hankel function of the first kind, $H_1^{(1)}$ is the first-order Hankel function of the first kind, $S(\omega)$ represents the source spectrum, k is the wavenumber of the propagating wavefield and $\eta(x')$ is the obliquity factor.

In the next chapter we are going to find an integral relationship to include the ghost reflection generated by the rough sea-surface to the modelled up-going wavefield. The down-going pressure wavefield (ghost) will be computed from the up-going vertical particle velocity wavefield and the rough free-surface reflectivity (or Green's function). The sea-surface will be computed based on Helmholtz-Kirchhoff integral (Orji et al., 2011).

Chapter 4

Data Modelling

In this chapter we follow Asgedom, Orji and Söllner (unpublished material) to derive based on Rayleigh's reciprocity theorem (Amundsen, 2001) an integral relationship to compute the down-going wavefield reflected from a rough free surface. Amundsen (2001) applied Rayleigh's reciprocity theorem to eliminate the free surface effects in marine seismic experiments by employing a physical state with free surface boundary and the actual seismic sources and a hypothetical state with virtual point sources and without the free surface boundary. He established an integral relationship between the desired (demultipled and designatured) pressure field and the recorded pressure and vertical velocity field containing all free-surface related multiples.

In this chapter, we exploit a similar principle to compute the down-going wavefield. This is achieved by first computing the sea-surface reflectivity based on Helmholtz-Kirchhoff integral technique (Orji et al., 2011) and combining this with up-going vertical particle velocity wavefield computed from any forward modelling software (Nucleus+).

Down-going Wavefield Computation

In this section the down-going wavefield will be computed for the actual receiver positions in a homogeneous layer by considering two cases:

1. When sources are above the receivers
2. When sources are below the receivers

4.1 Case1: When Sources are above the Receivers

In this case two states have been considered, one physical state (state A) and one hypothetical state (state B). The main aim is to relate these two states. Geometry of physical state (state A) and hypothetical state (state B) are shown in Figure 4.1 and Figure 4.2. The volume V is bounded by hemisphere S_R with radius r' (that goes to infinity) and connecting level $Z = Z^l$ (which is not a physical boundary) is the same in two experiments. The volume-V consists of air-water surface S_0, a water layer, receivers and sources (above the receivers) but the solid subsurface (indicated by α) below the water layer is outside the volume. In the physical marine seismic experiment (state A), the source array is shown by $\mathbf{X}_{S_i}$. There are only up-going wavefields in this actual state and it contains all the reflection from the subsurface. The actual receiver is at $\mathbf{X}_R$ where the data is recorded but the reciprocity relation connects the pressure and velocity wavefields of both states at level $Z = Z^l$. The level $Z = Z^l$ is also the level where the wavefield separation takes place.

State A
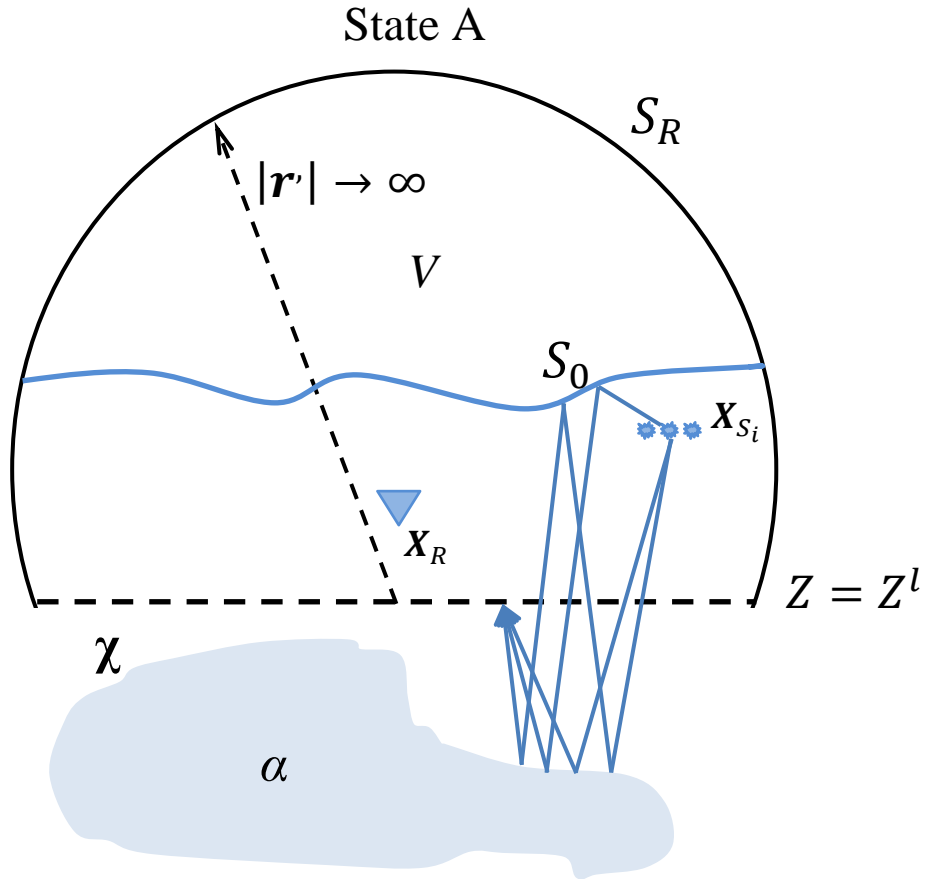
Figure 4.1: Geometry of physical marine seismic experiment. The volume V is defined by the hemisphere S_R and nonphysical boundary $Z = Z^l$. The source is located at the center position of $\mathbf{X}_{S_i}$ and the receiver is below the source $Z_R > Z_S$ at location $\mathbf{X}_R$. The up-going waves are reflected downwards from sea-surface which lead to generation of multiples.

The physical (actual) state is described by

Fields: $\{P_A, V_{ZA}\}$,

Sources: $\sum S_i \rho^{-1}(X)\delta(X - X_{S_i})$,

where ρ is volume density of mass, P_A is acoustic pressure and V_{ZA} is particle velocity. S_i is the signature for that individual array of guns.

In state B or hypothetical state there is only the sea-surface but not the subsurface reflectors (the medium below the connecting level $Z = Z^l$ is homogeneous). The hypothetical source is located at the actual receiver location $\mathbf{X}_R$. In this case again we interested in the wavefields at the connecting level. So the wave can propagate directly from source to this level or can be scattered at the sea-surface and come down that are shown by the red arrows at Figure 4.2. The virtual receivers are located at $\mathbf{X}_S$. In the actual state (state A) the actual sources are inside the volume V, thus in the hypothetical state we need to model the wavefield going from the virtual sources to their corresponding receivers (shown by solid black arrows in Figure 4.2).
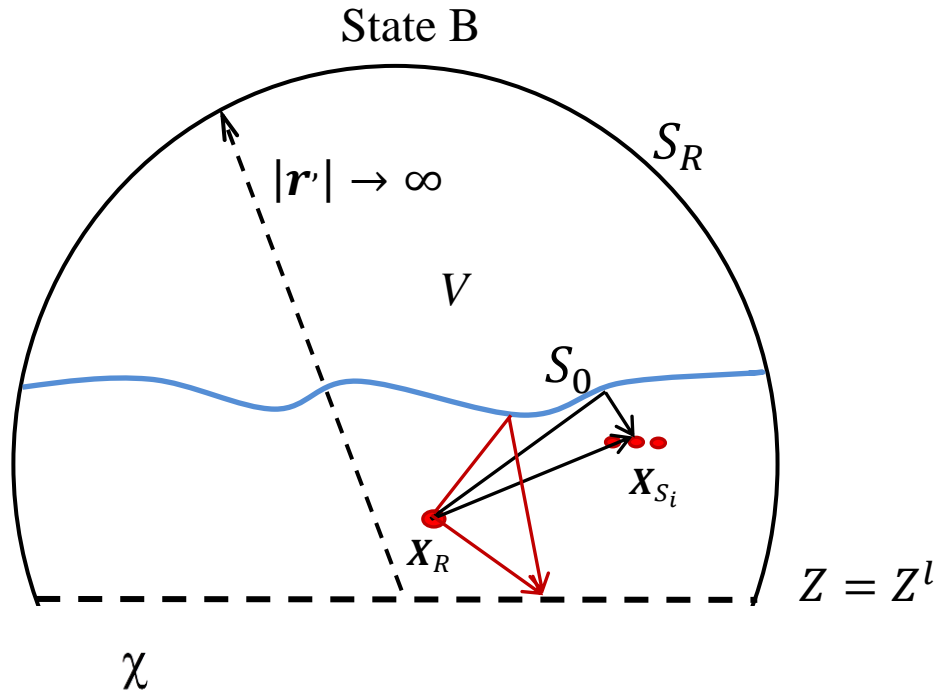
Figure 4.2: Geometry of hypothetical marine seismic experiment. The volume V is the same as state A. The source is located at the position of $\mathbf{X}_R$ and receiver is above the source at location $\mathbf{X}_{S_i}$. The direct wave from the source to the receiver and its ghost are shown by black arrows. The wave from the source to the level $Z = Z^l$ and the source ghost to this level has shown by red arrows.

The hypothetical state is described by

Fields: $\{P_B, V_{ZB}\}$,

Sources: $S^d \rho^{-1}(X)\delta(X - X_R)$,

where ρ is volume density of mass, P_B is acoustic pressure and V_{ZB} is particle velocity. S^d is the signature for the point source in hypothetical state.

From Rayleigh's reciprocity theorem (given in appendix A):

$$-\frac{S^d}{\rho(X_R)} P_A(X_R, X_S) + \sum_{i=1}^{N} \frac{S_i}{\rho(X_{S_i})} P_B(X_{S_i}, X_R) =$$

$$i\omega \int \Big(P_B(X, Z^l \mid X_R) v_A(X, Z^l \mid X_S)$$

$$- P_A(X, Z^l \mid X_S) v_B(X, Z^l \mid X_R) \Big) dX, \qquad (4.1.1)$$

where X is the x-coordinate and Z^l is the depth where the fields in state A and B are recorded.

The first term on the right hand-side of the Eq. (4.1.1) is the pressure recorded at the connecting level from the virtual source at X_R multiplied by the particle velocity recorded at the connecting level from the actual source at X_s. The second term on the right hand-side of the Eq. (4.1.1) is the pressure recorded at the connecting level from the actual source at X_S multiplied by the particle velocity recorded at the connecting level from the virtual source at X_R. The second term on the left hand-side of Eq. (4.1.1) is the direct wave from the virtual source at $\mathbf{X}_R$ to the corresponding virtual receivers at $\mathbf{X}_{si}$. The first term in Eq (4.1.1) gives the pressure wavefield at a given position inside the volume (i.e. $\mathbf{X}_R$) as a result of the direct wave and the contribution from surface integral (i.e all the external sources).

The integral relation from Eq. (4.1.1) will now be expressed by separated wavefields as derived by Wapenaar and Berkhout (1989). The wavefield separation is taken at the connecting level. The propagated waves in opposite directions interact at $Z = Z^l$. The total pressure is decomposed into down-going wavefield P_B^+ and up-going wavefield P_B^-.

$$P_B = P_B^+ + P_B^-.$$

The total z-component of the particle velocity wavefield is decomposed into up-going velocity v_{ZA}^- and down-going velocity v_{ZA}^+ :

$$v_A = v_{ZA}^+ + v_{ZA}^-.$$

The new integral relation reads:

$$-S^d P_A(X_R, X_S) + \sum_{i=1}^{N} S_i\, P_B(X_{S_i}, X_R)$$

$$= 2i\omega\rho \int \Big(P_B^-(X, Z^l \mid X_R) v_{ZA}^+(X, Z^l \mid X_S)$$

$$+ P_B^+(X, Z^l \mid X_R) v_{ZA}^-(X, Z^l \mid X_S) \Big) dX, \qquad (4.1.2)$$

For $Z_R < Z^l$, $P_B^-(X, Z^l \mid X_R) = 0$ (There is no up-going wave at the separation level in the hypothetical state). This leads to

$$-S^d P_A(X_R, X_S) + \sum_{i=1}^{N} S_i\, P_B(X_{S_i}, X_R)$$

$$= 2i\omega\rho \int \Big(P_B^+(X, Z^l \mid X_R) v_{ZA}^-(X, Z^l \mid X_S) \Big) dX, (4.1.3)$$

Rearranging the Eq. (4.1.3):

$$S^d P_A(X_R, X_S)$$

$$= \sum_{i=1}^{N} S_i\, P_B(X_{S_i}, X_R)$$

$$- 2i\omega\rho \int \Big(P_B^+(X, Z^l \mid X_R) v_{ZA}^-(X, Z^l \mid X_S) \Big) dX, (4.1.4)$$

Applying source receiver reciprocity in state B (i.e. the source and receiver positions are interchanged so that sources become receivers and the receivers become sources). Thus as it can be seen in Figure 4.3 the direction of the arrows has been changed. In this stage we have both the down-going and up-going pressure $P_B^{-,+}$.

$$S^d P_A(X_R, X_S)$$

$$= \sum_{i=1}^{N} S_i\, P_B\big(X_R, X_{S_i}\big)$$

$$- 2i\omega\rho \int \Big(P_B^{-,+}(X_R \mid X, Z^l) v_{zA}^-(X, Z^l \mid X_S) \Big)\, dX,$$

(4.1.5)
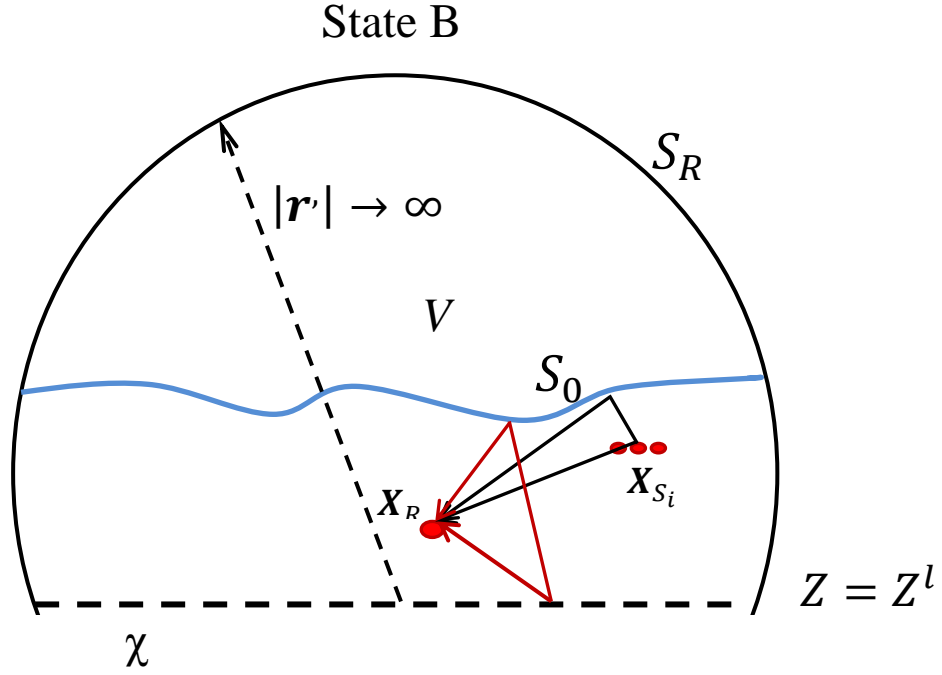
State B

Figure 4.3: Geometry of hypothetical marine seismic experiment. By applying the source receiver reciprocity in state B the direction of arrows has been changed from source at the position X_{S_i} to the receiver at X_R position.

Taking only the down-going wavefield at the receiver level, Eq. (4.1.5) reduces to:

$$S^d P_A^+(X_R, X_S)$$

$$= \sum_{i=1}^{N} S_i\, P_B\big(X_R, X_{S_i}\big)$$

$$- 2i\omega\rho \int \Big(P_B^+(X_R \mid X, Z^l) v_{zA}^-(X, Z^l \mid X_S) \Big)\, dX,$$

(4.1.6)
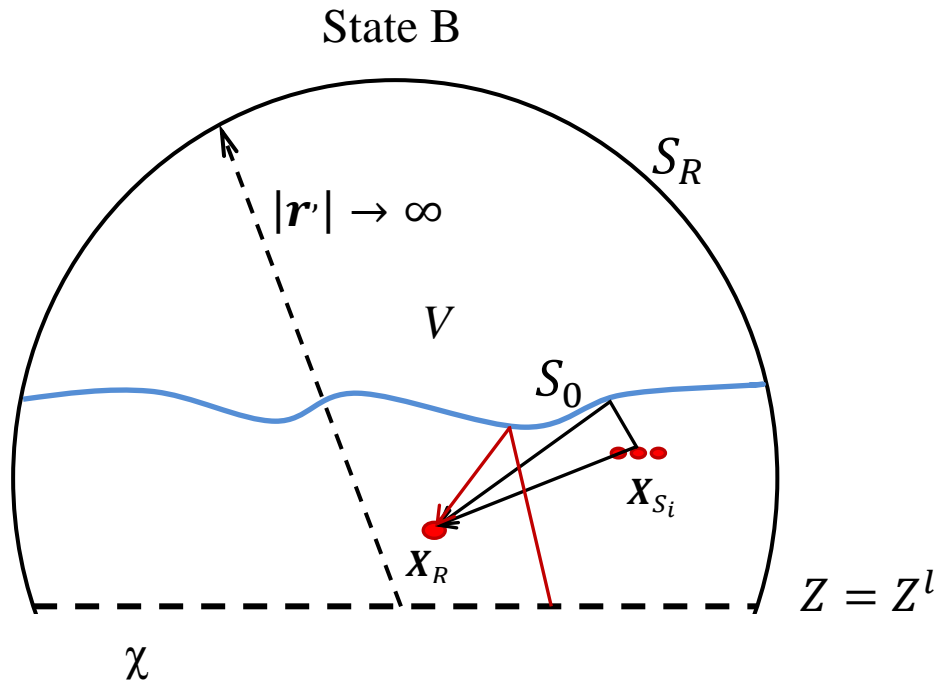
Figure 4.4: Geometry of hypothetical marine seismic experiment after applying the source receiver reciprocity in state B. It contains the direct wave from source to receiver and the source ghost and the up-going wave from the connecting level to the receiver that is scattered from sea-surface.

By using Eq. (4.1.6) the down-going wavefield can be computed. This equation gives the integral relationship between the down-going pressure and up-going vertical component of the particle velocity with reflected wavefield in the hypothetical state. The first term in the left-hand side of the Eq. (4.1.6) is the direct wave from source to receiver. This is kept because the location of the source is above the receiver. For the calculation of the down-going pressure wavefield, the up-going velocity is generated by modelling at a given source and recorded at   receivers located at the separation level. In the case of source above the receiver, first we need to model the direct pressure wavefield from the actual source to the receiver position (including the source ghost) and second, the down-going pressure wavefield (of the hypothetical state) at the actual receiver from sources at the separation level. The latter wavefield involve the computation of the sea-surface reflectivity.

4.1.1 Physical Interpretation for Down-going Wavefield Computation

For the case when sources are above the receivers, two states have been considered, state A or physical experiment and state B or hypothetical experiment. We can see the up-going wave with blue color in state A which is the up-going velocity data (e.g. modelled with the software Nucleus+). The sea-surface reflectivity shown with red line (i.e. modelled using Kirchhoff-Helmholtz integral) and the direct wave with its source ghost (black line) are in state B.

By using the integration Eq. (4.1.6), the sea surface reflectivity is connected to the up-going vertical velocity at the connecting level. A generated wave at the source location X_S goes down to the subsurface, when it comes up (the blue line) it gets connected at the connecting level to the reflectivity (red color) get reflected from sea surface and become a down-going wavefield.
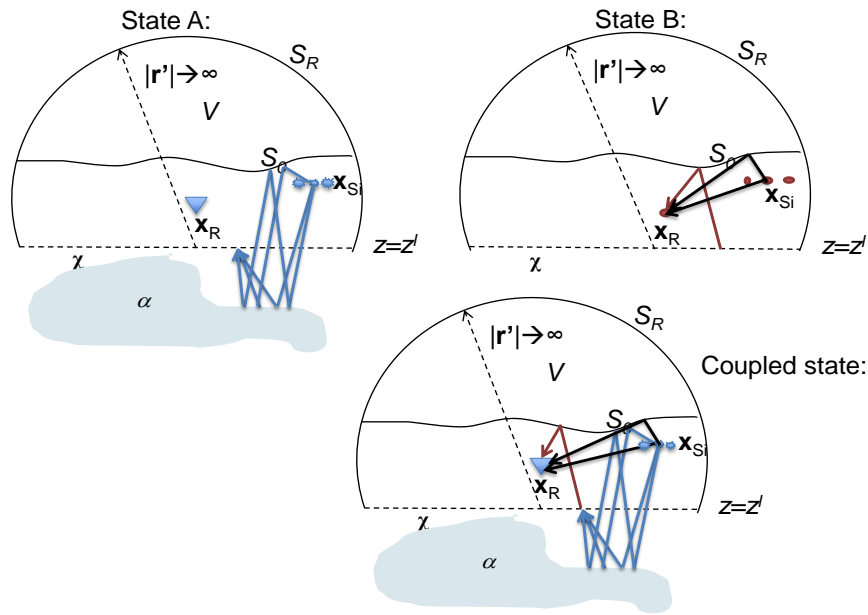
Figure 4.5: Geometry of seismic experiments: state A or actual state, state B or hypothetical state and the coupled state which is the combination of sate A and B.

4.2 Case2: When Sources are below the Receivers

In the case when the sources are below the receivers, we consider two states, physical experiment (state A) and hypothetical experiment (state B). The same aim as case1 has been followed here which is relating these two states. Geometry of physical state (state A) and hypothetical state (state B) are shown in Figure 4.6 and Figure 4.7. In both states the volume V is bounded by hemisphere S_R with radius $r^\prime$ (that goes to infinity) and connecting level $Z = Z^l$ as a nonphysical boundary that can be in any depth between the actual sources and receivers.

In the physical experiment (state A) the volume V consists of air-water surface S_0, a water layer, receivers but not the sources and the solid subsurface (indicated by α) below the water layer. The source array is shown by $\mathbf{X}_{S_i}$. The actual receiver is located at $\mathbf{X}_R$ where the data is recorded the reciprocity relation connects the pressure and velocity wavefields of both states at level $Z = Z^l$ where the wavefield separation takes place.
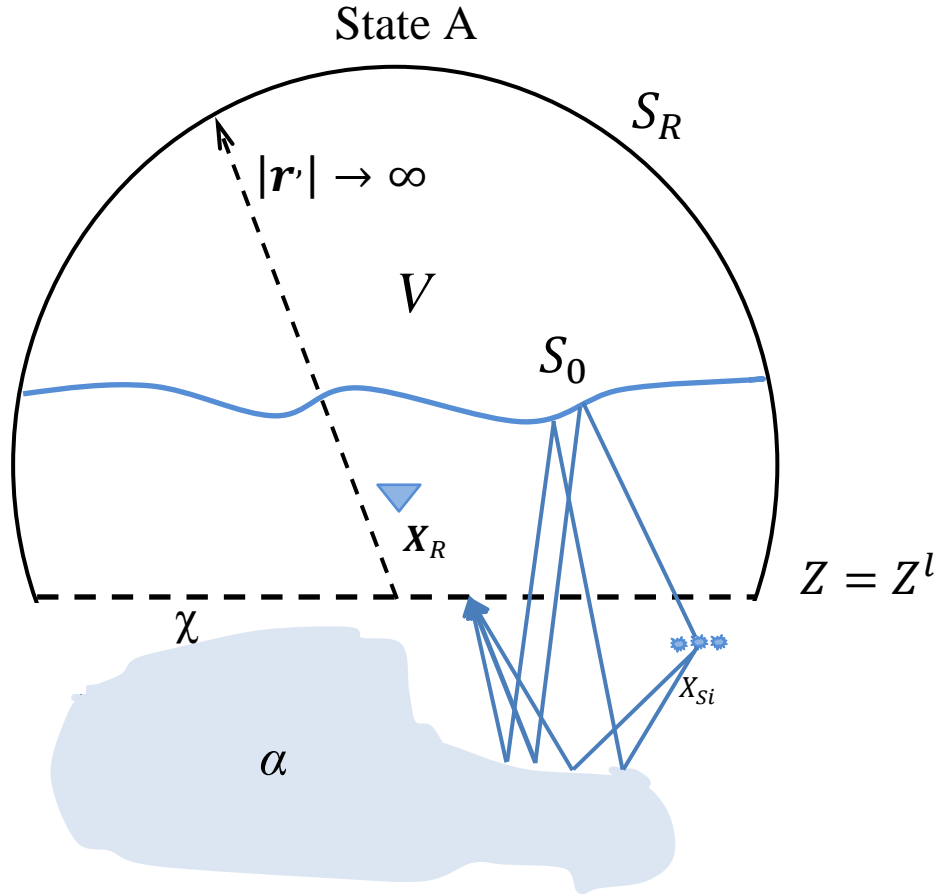
Figure 4.6: Geometry of physical marine seismic experiment. The volume V is defined by the hemisphere S_R and nonphysical boundary $Z = Z^l$. The receiver is located at the $\mathbf{X}_R$ position above the source at the center position of $\mathbf{X}_{S_i}$, $Z_S > Z_R$. The up-going waves are reflected downwards from sea surface which lead to generation of multiples.

The physical (actual) state is described by

Fields: $\{P_A, V_{ZA}\}$,

Sources: 0,

where P_A is acoustic pressure and V_{ZA} is particle velocity. The seismic source is located outside of the volume so it is zero.

In state B or hypothetical state the volume V consist of the sea surface S_0 but not the subsurface reflectors. The hypothetical source is located at the actual receiver location $\mathbf{X}_R$. The data is recorded at connecting level. The waves can propagate directly from source to the connecting level or can be scattered at the sea surface and come down to this level that are shown by the red arrows in Figure 4.7.
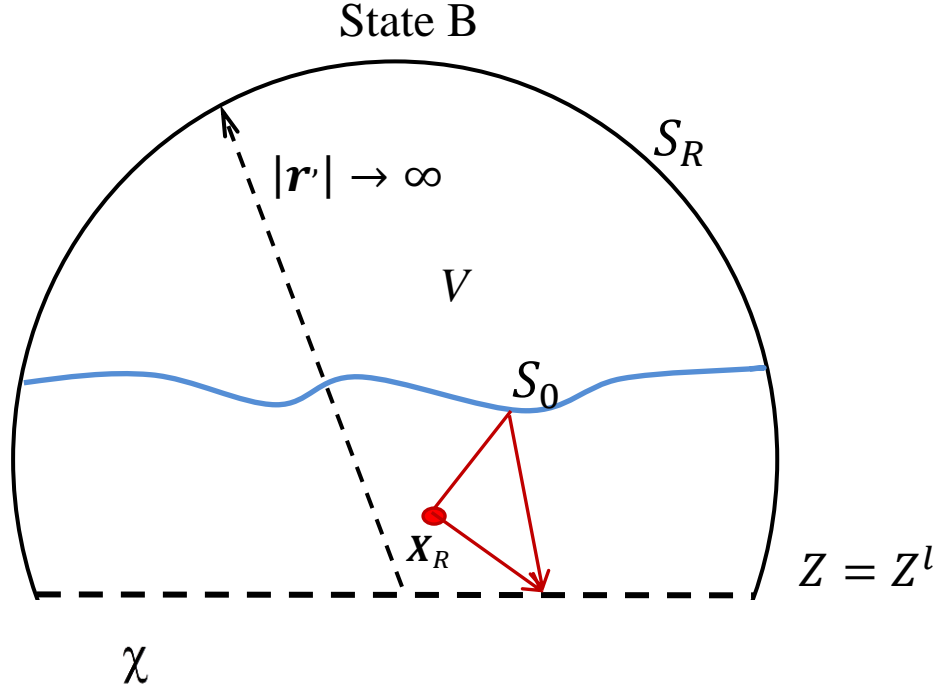
Figure 4.7: Geometry of the hypothetical marine seismic experiment. The volume V is the same as state A. The source is located at the position of $\mathbf{X}_R$ inside the volume and the receiver at the location $\mathbf{X}_{Si}$ outside of the volume V below the receiver.

Fields: $\{P_B, V_{ZB}\}$,

Sources: $S^d \rho^{-1}(X)\delta(X - X_R)$,

where ρ is volume density of mass, P_B is acoustic pressure and V_{ZB} is particle velocity. S^d is the signature for the point source in hypothetical state.

Applying Rayleigh's reciprocity theorem:

$$-\frac{S^d}{\rho(X_R)}P_A(X_R, X_S) =$$

$$i\omega \int \Big(P_B(X, Z^l \mid X_R)v_A(X, Z^l \mid X_S)$$

$$- P_A(X, Z^l \mid X_S)v_B(X, Z^l \mid X_R) \Big) dX, \qquad (4.2.1)$$

where X is the x-coordinate and Z^l is the depth where the pressure in state B from source in X_R is recorded.

Rewriting Eq. (4.2.1) using separated wavefields (Wapenaar and Berkhout, 1989):

$$
\begin{aligned}
-S^d P_A(X_R, X_S) \\
= 2i\omega\rho \int \Big(P_B^-(X, Z^l \mid X_R) v_{ZA}^+(X, Z^l \mid X_S) \\
+ P_B^+(X, Z^l \mid X_R) v_{zA}^-(X, Z^l \mid X_S) \Big) dX,
\end{aligned}
\tag{4.2.2}
$$

For $Z_R < Z^l \quad P_B^-(X, Z^l \mid X_R) = 0,$ \hfill (4.2.3)

$$
-S^d P_A(X_R, X_S) = 2i\omega\rho \int \Big(P_B^+(X, Z^l \mid X_R) v_{zA}^-(X, Z^l \mid X_S) \Big) dX,
\tag{4.2.4}
$$

Applying source receiver reciprocity in state B:

$$
S^d P_A(X_R, X_S) = -2i\omega\rho \int \Big(P_B^{-,+}(X_R \mid X, Z^l) v_{zA}^-(X, Z^l \mid X_S) \Big) dX,
\tag{4.2.5}
$$
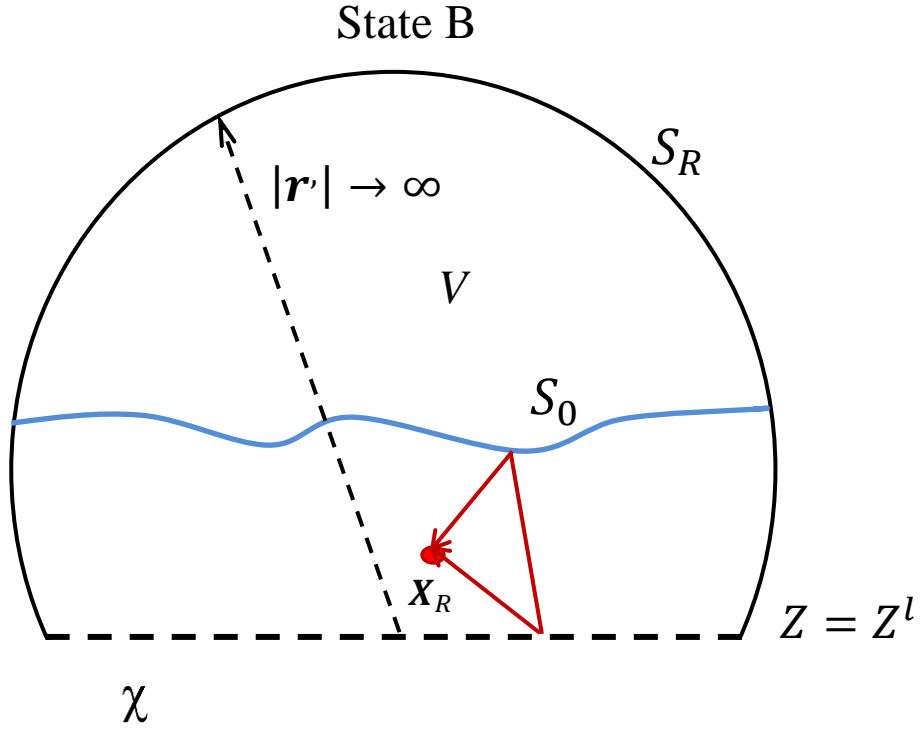
Figure 4.8: Geometry of hypothetical marine seismic experiment. After applying the source receiver reciprocity in state B the location of the source and receiver are replaced. The direction of arrows has been changed. The waves go up from Z^l level direct to the receiver position X_R or are scattered at the sea-surface and recorded at the receiver.

Keeping only the down-going wavefields:

$$S^d P_A^+(X_R, X_S) = -2i\omega\rho \int \left(P_B^+(X_R \mid X, Z^l) v_{zA}^-(X, Z^l \mid X_S) \right) dX, \tag{4.2.6}$$

Eq. (4.2.6) is the same as Eq. (4.1.6), except that there is additional direct wave contribution in Eq. (4.1.6). To compute the down-going pressure wavefield in the case when the sources are below the receivers, the up-going velocity is generated by modelling at a given source and recorded at receivers located at the separation level. We need to model the down-going pressure wavefield (or the sea-surface reflectivity) at the actual receiver from sources at the separation level.
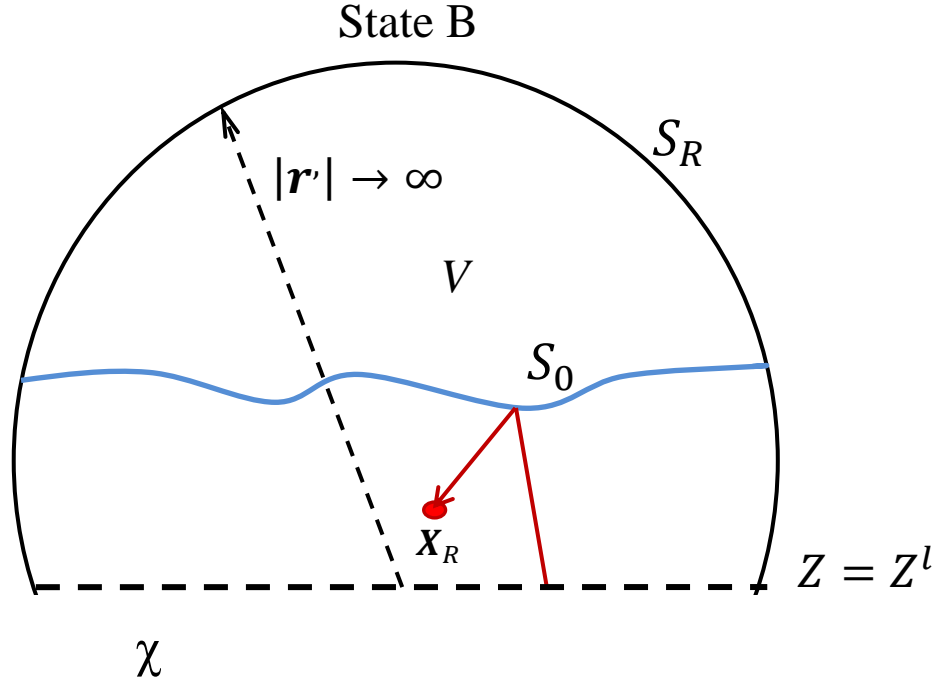
Figure 4.9: Geometry of the hypothetical marine seismic experiment. After applying the source receiver reciprocity in state B the location of the source and receiver are source receiver reciprocity in state B the location of the source and receiver are replaced. The direction of arrow has been changed. Here we take only the up-going waves from Z^l level that are scattered at the sea-surface and recorded at the receiver.

4.2.1 Physical Interpretation for Down-going Wavefield Computation

We consider two states, state A or physical state and state B or hypothetical state. The up-going waves (velocity data) are shown with blue color in the physical experiment (state A) and the reflectivity with red lines in state B. By using the integration Eq. (4.2.6) the sea-surface reflectivity is connected to the up-going vertical velocity at the connecting level. A wave generated at source location goes down to the subsurface; when it comes up (the blue line) it gets connected at the connecting level to the reflectivity (red color) and then gets recorded by the receiver (see Figure 4.10).
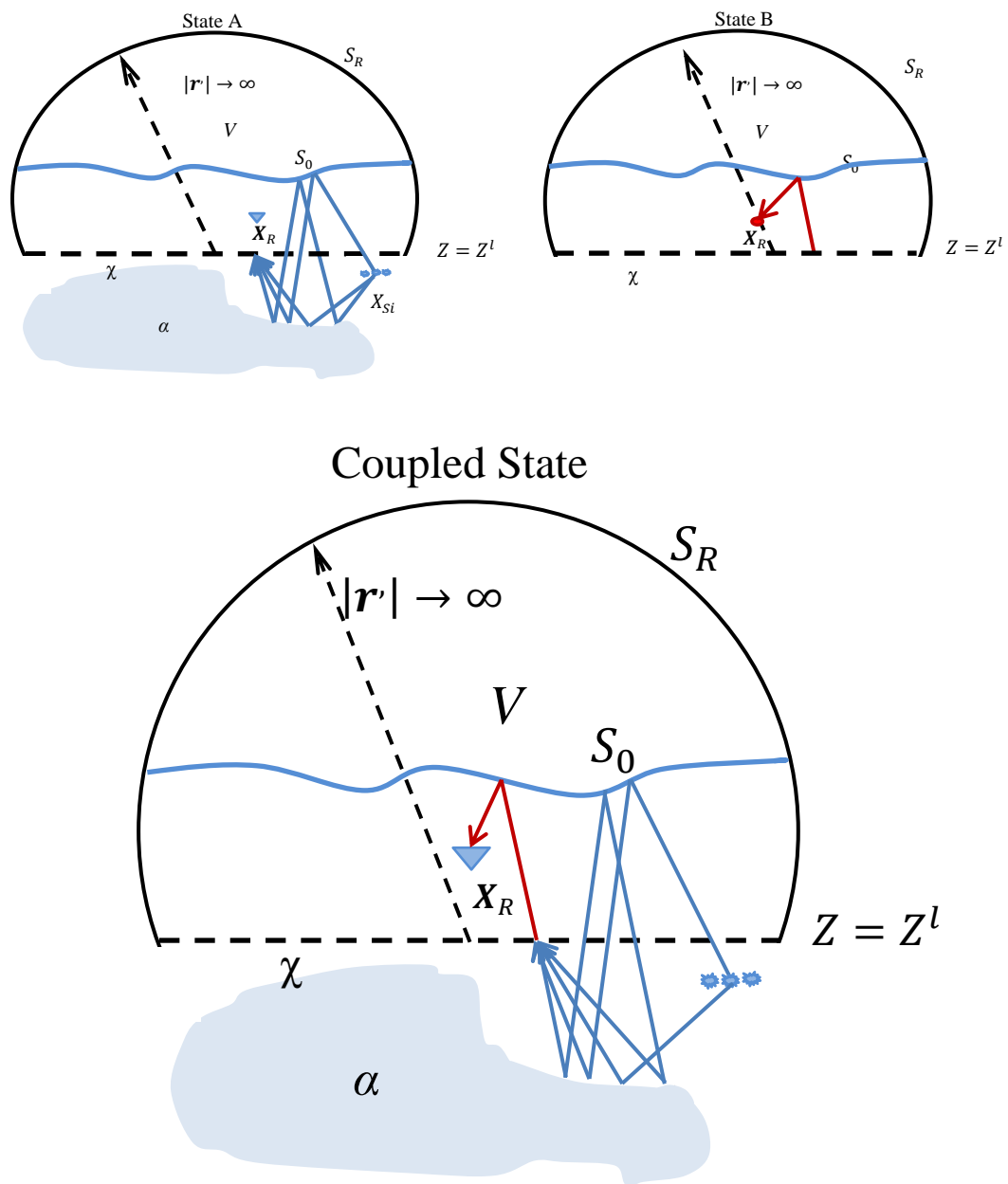
Figure 4.10: Geometry of seismic experiments, state A or actual state, state B or hypothetical state and coupled state which is the combination of state A and state with the source below the receiver.

Chapter 5

Synthetic Data Examples

In this chapter we validate the computation of the down-going pressure wavefield from a given sea-surface using synthetic data modeled with Nucleus+, the PGS proprietary software. Three different sea-surface shapes are considered; flat, sinusoidal and rough sea-surface based on Pierson-Moscowitz spectral model.

5.1 Data Generation by Nucleus+

Synthetic data generation with Nucleus+ software starts with the generation of a vessel (cf. Figure 5.1 and 5.3), where we selected a single air gun as our seismic source and a single line Geostreamer cable as our receiver. The source is located at 400 m from the vessel in the in line direction and at a depth of 106 m. Ricker wavelet is used as a source signature.

Figure 5.1 shows the plot of a vessel with a towed source and streamer. The time function, amplitude spectrum and phase spectrum plot of this signature can be seen in Figure 5.2. Figure 5.3 shows a table of the vessel parameters.

The streamer contains 128 dual sensors (i.e. hydrophone and geophone) placed with spacing of 6.25 m and at a depth of 100 m. The recorded data has a recording length of 2046 ms and a sampling interval of 2 ms.
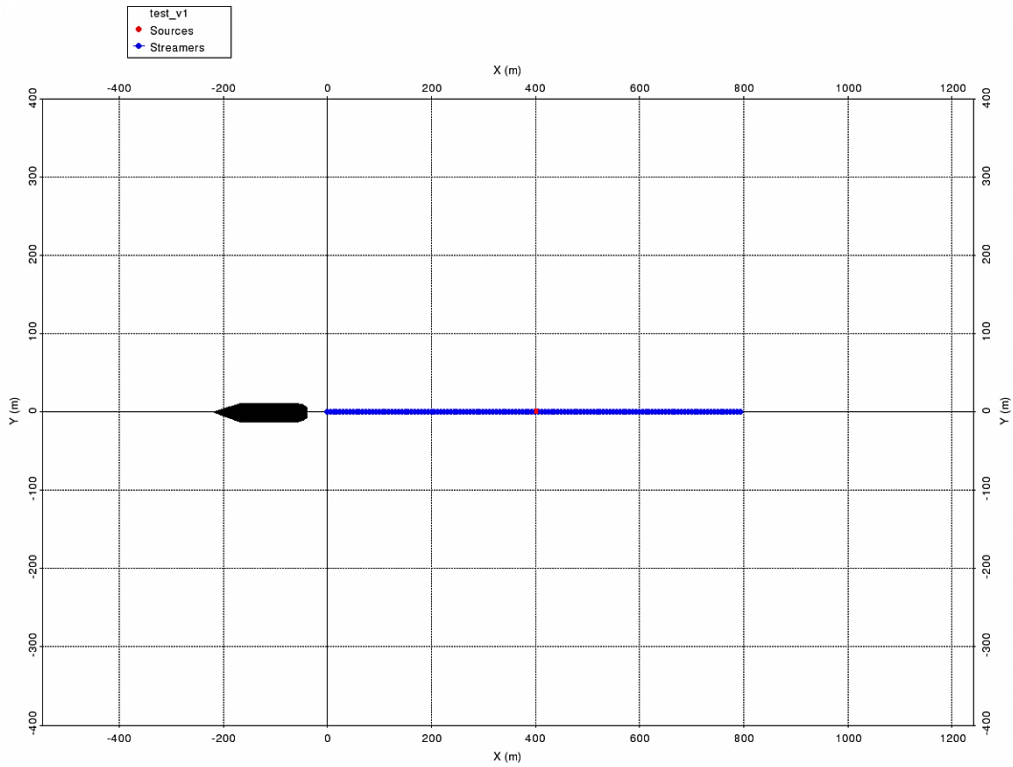
Figure 5.1: Plot of a vessel with a towed source (red color) and streamer (blue color).
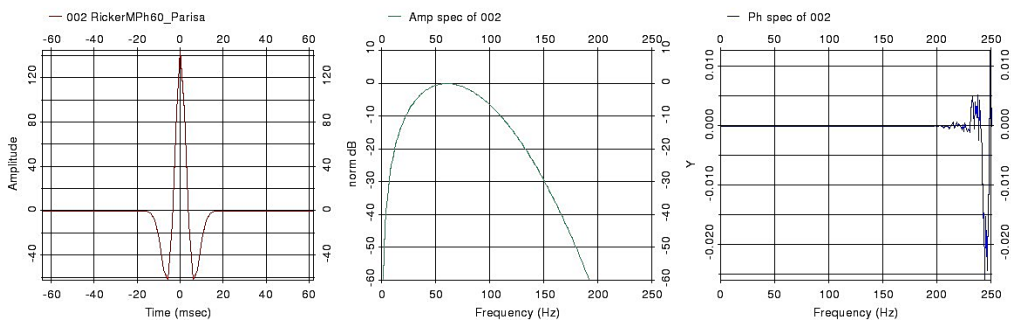
Figure 5.2: A plot of the time-function, amplitude spectrum and phase spectrum of the source signature.

44

VESSEL PARAMETERS :

Project : test_parisa1
Dataset : test_v1

Sample interval (ms) : 2.0
Recording length (ms) : 2046.0

Source array   : RickerMPh60_Parisa
Recording filter   : No filter applied
Filter frequencies (Hz) :   0.0   180.0
Filter slopes (dB/oct)   :   18.0   18.0

Number of sources   : 1
Source depth (m)   : 106.0
Shot point distance (m) : 25.0
Sub surface line sep. (m) : 25.0
Sail line separation (m) : 25.0

Number of streamers : 1
Streamer type   : Geostreamer
Streamer depth (m) : 100.0
No. groups/streamer : 128
Group interval (m) : 6.2
Type of feathering : None
Stack fold   : 16

Hydrophone array description : Regular
Number of hydrophones   : 8
Hydrophone group length (m) : 6.2

Geophone array description : Regular
Number of geophones   : 8
Geophone group length (m) : 6.2

Positions of sources :

Number   X   Y   Sequence
  1   400.0   0.00   1

Position of first receiver on streamer :

Number   X   Y   Feather
  1   0.00   0.00   0.00

Figure 5.3: Table of the vessel parameter.

5.2 Definition of the Controlled Model

The earth model is horizontally layered with 3 interfaces. The first interface is the air-water (sea-surface) interface at 0 m, the second interface (or the sea floor) is at a depth of 1000 m and the last interface (or geological boundary) is at a depth of 1200 m. The last layer in the model is a half space. The layers specified P-wave velocities and densities are listed below:

1. The first layer (air) $V_P = 333\ ^m/_s, \rho = 0.0\ ^g/_{cm^3}$,
2. The second layer (water) $V_P = 1500\ ^m/_s, \rho = 1.0\ ^g/_{cm^3}$,
3. The third layer (sediment) $V_P = 2000\ ^m/_s, \rho = 1.0\ ^g/_{cm^3}$,
4. The last layer (sediment) $V_P = 2200\ ^m/_s$, $\rho = 1.0\ ^g/_{cm^3}$, (half space).

The total size of this 2-D horizontal plane layer model is 1500 both in lateral and vertical direction (see Fig. 5.4).
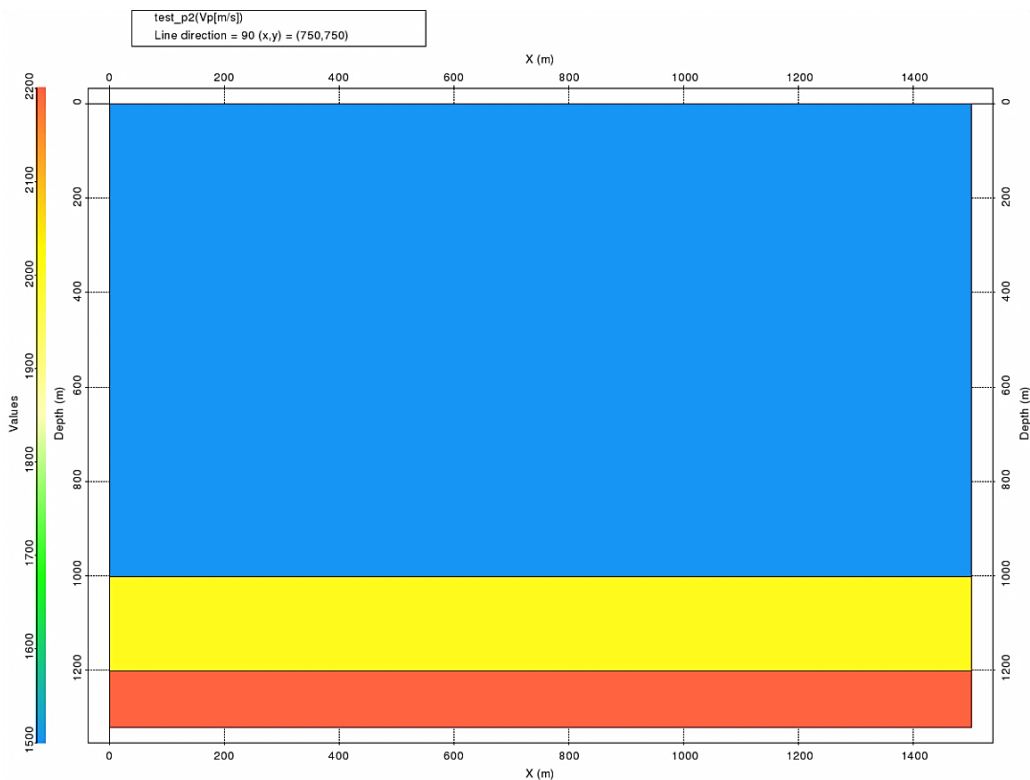
Figure 5.4: The 2-D horizontal plane layer model showing the P-wave velocities.

To acquire a data, we first need to define the survey, which can be a point survey (the survey is defined by one single CMP point) if only one point to be surveyed, or a line survey (means that the survey is defined by CMP points on

a single straight line) or an area survey which is defined by a number of three or more points (corner points) defining the area of the survey. The coordinates of the survey are defined based on the UTM coordinate system. For our study we selected a point survey with East and North coordinates as 450 m, and 400 m respectively. The plot of the point survey can be seen in Figure 5.5. Figure 5.6 shows the table of the streamer point survey's parameters.
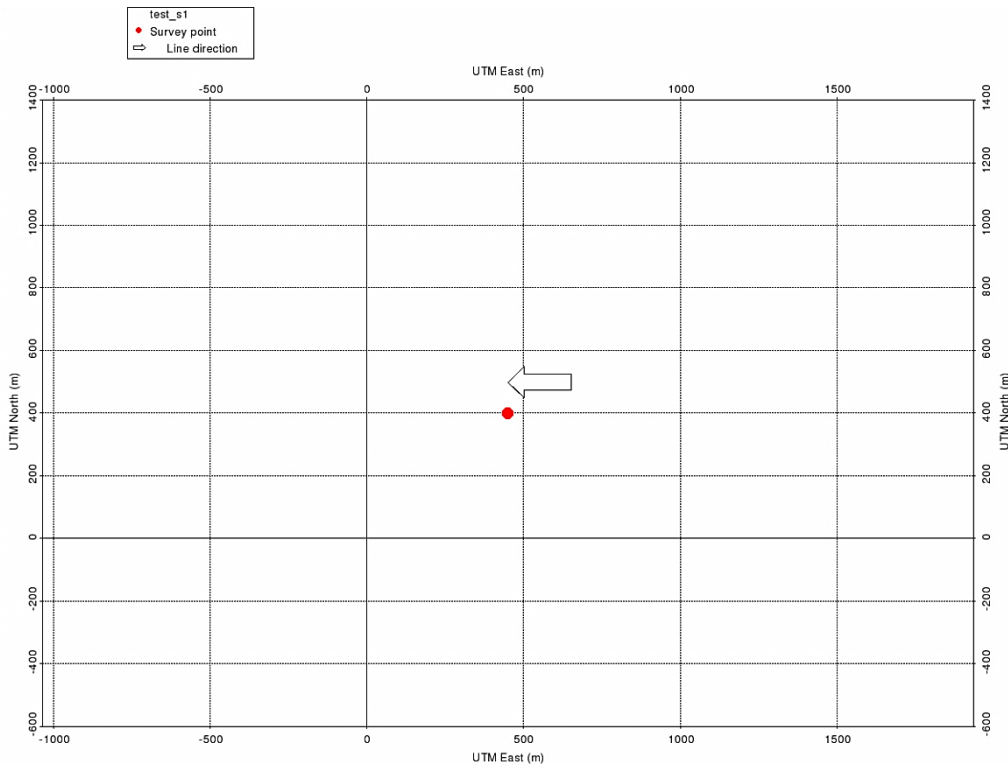
Figure 5.5: Plot of the survey in the UTM coordinate system with its direction (Streamer point survey).

Streamer point survey
Project : test_parisa1 Name   : test_s1 Line direction (degree) : 270 Coordinates (east, north) : 450 , 400

Figure 5.6: Table of streamer point survey parameter.

After defining all the necessary acquisition parameters, we generated a synthetic data using the Ray-tracing method. Figure 5.7 shows the ray path from the source to the reflectors and back to the receivers.
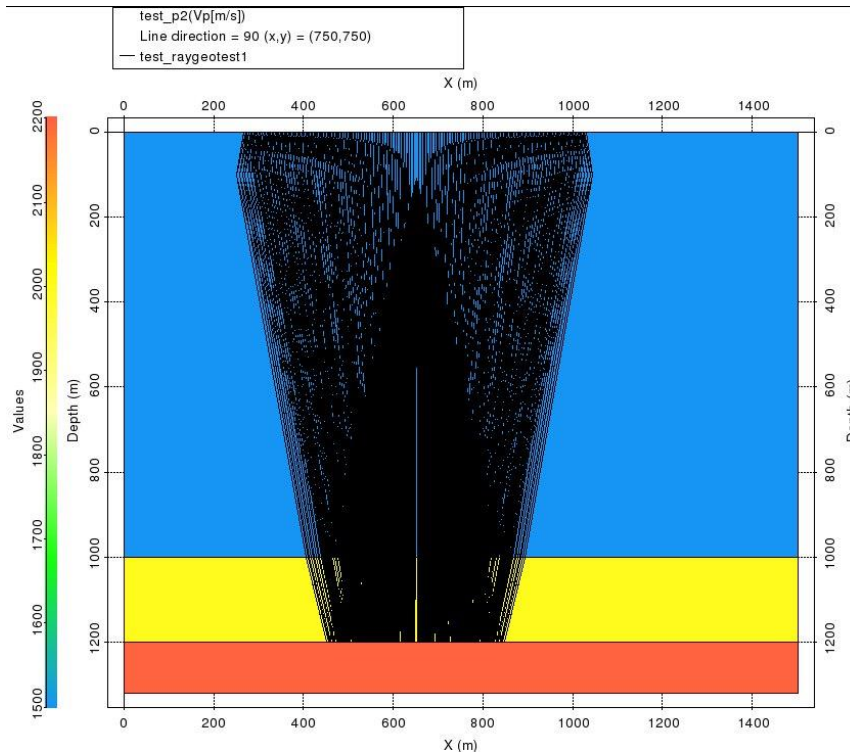
Figure 5.7: The event data plot which shows the ray paths from the source to 128 receivers.

The ghost reflection at the receiver side is shown in Figure 5.8. Here, for the sake of clarity we only show the ray path involving the first receiver.
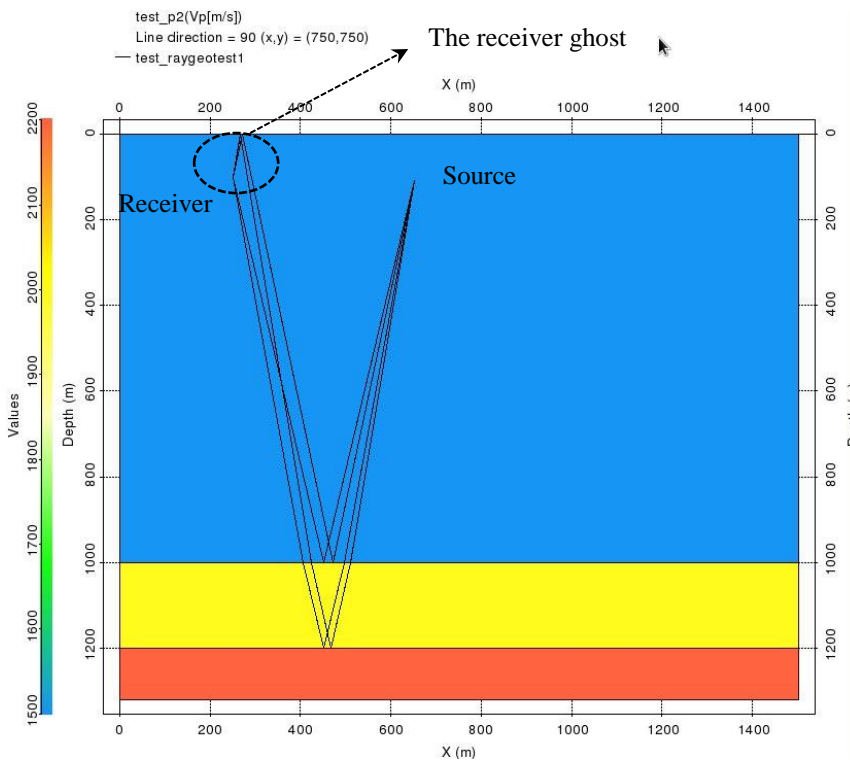
Figure 5.8: The event data plot which shows the ray paths for one receiver.

Utilizing the event data obtained from the ray-tracing both hydrophone and geophone data were generated (c.f. Figure 5.9-5.11). The up-going and down-going pressure wavefields from the first and second reflector are indicated by the arrows in the Figure 5.9.
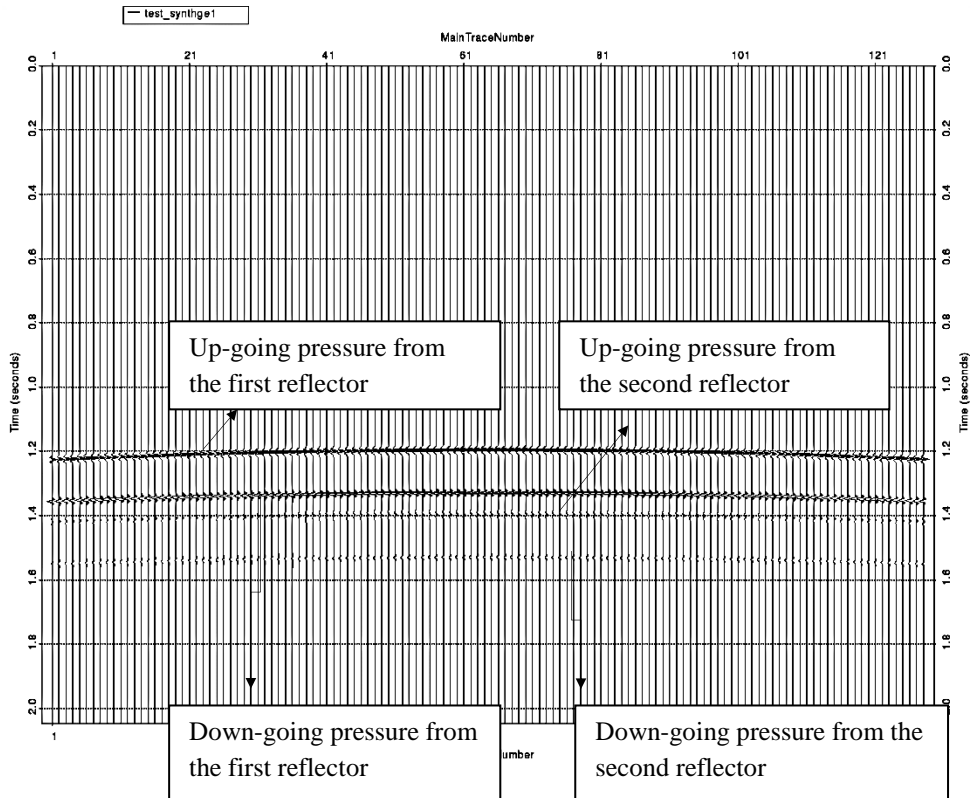
Figure 5.9: Synthetic total pressure data modeled with Nucleus+.

Figure 5.10 shows the synthetic data from Figure 5.9 in large scale. The reverse polarity between the up-going and down-going pressure from both the first and second reflector can be seen clearly in this Figure.
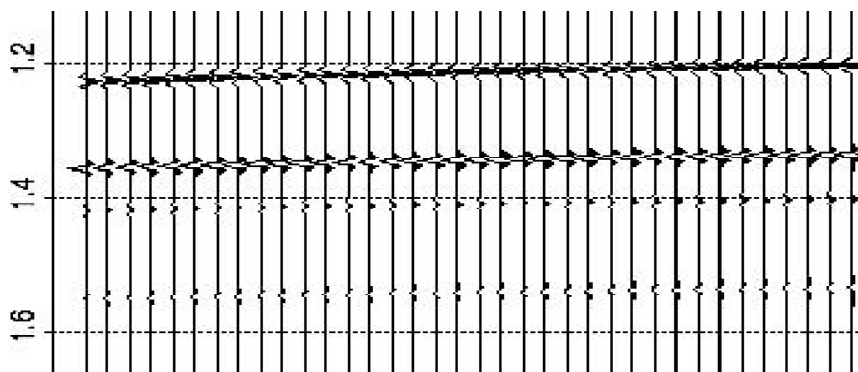
Figure 5.10: The synthetic data in large scale to show the reverse polarity between the up-going and down-going pressure wavefield from the first and second reflector at subsurface.

The up-going particle velocity data, required for the reconstruction of the down-going pressure field, is shown in Figure 5.11.
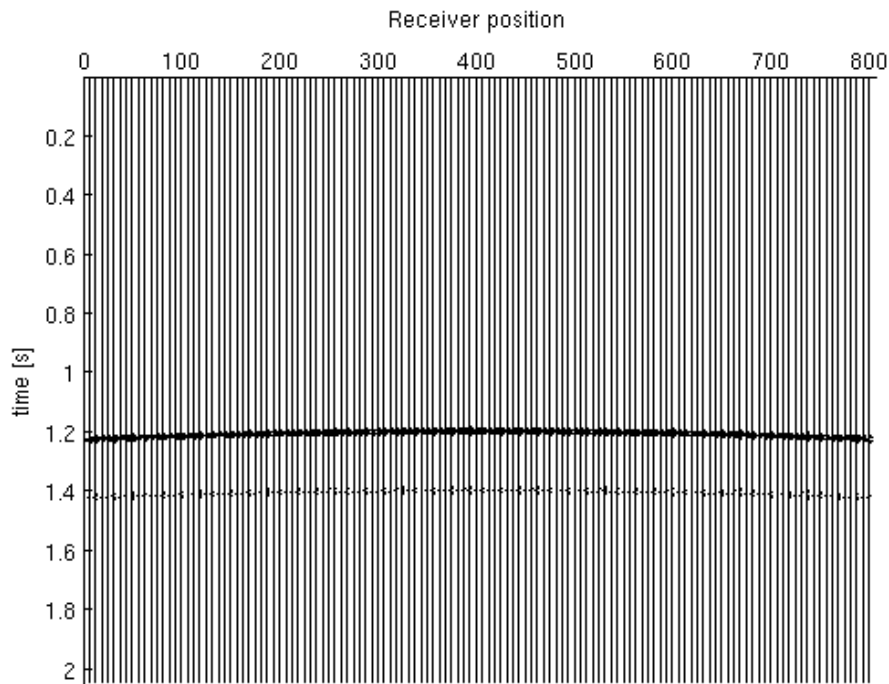
Figure 5.11: The up-going wavefield recorded by geophones from Nucleus+.

Traces are displayed in time-receiver (sensor) position plot.

5.3 Modelling the flat Sea-Surface Response

The down-going wavefield referred to the response of the surface or the ghost signal. In a marine seismic survey, when the source fires some of the waves travel downward to the sea floor where they are reflected by the seismic reflectors at the subsurface. The reflected waves from the sea floor travel upward to the air-water interface (up-going wavefield), and at the travel path toward the sea-surface are recorded by the receivers. The up-going wavefields continue propagating upward before being reflected downward from the water surface with a reverse polarity and again are detected by the sensors on the streamer (down-going wavefield). The receivers (dual-sensor) record the reflected down-going (time-delayed) wavefield from the sea-surface (ghost) and the up-going wavefield from the sea floor, simultaneously. For modelling the sea-surface response (refer to Figure 4.9 in chapter 4) the ideal seismic

source which is a "spike" is considered at the same position of the receivers (c.f. Figure 5.12-5.15). Firstly, the source is considered over the position of the first receiver on the streamer (see Figure 5.13). Figure 5.14 shows the ray paths from the source supposed at the first receiver position along the streamer to the sea-surface (up-going wavefield) and the reflected rays or ghost reflection from the air-water interface to the sensors (down-going wavefield).

Then the source moves forward to the next receiver position (see Figure 5.15) and this process will proceed up to end (128 positions), for each source the response is calculated for all the receivers. The sea-surface response is computed based on Helmholtz-Kirchhoff integral method (Orji et al., 2011).
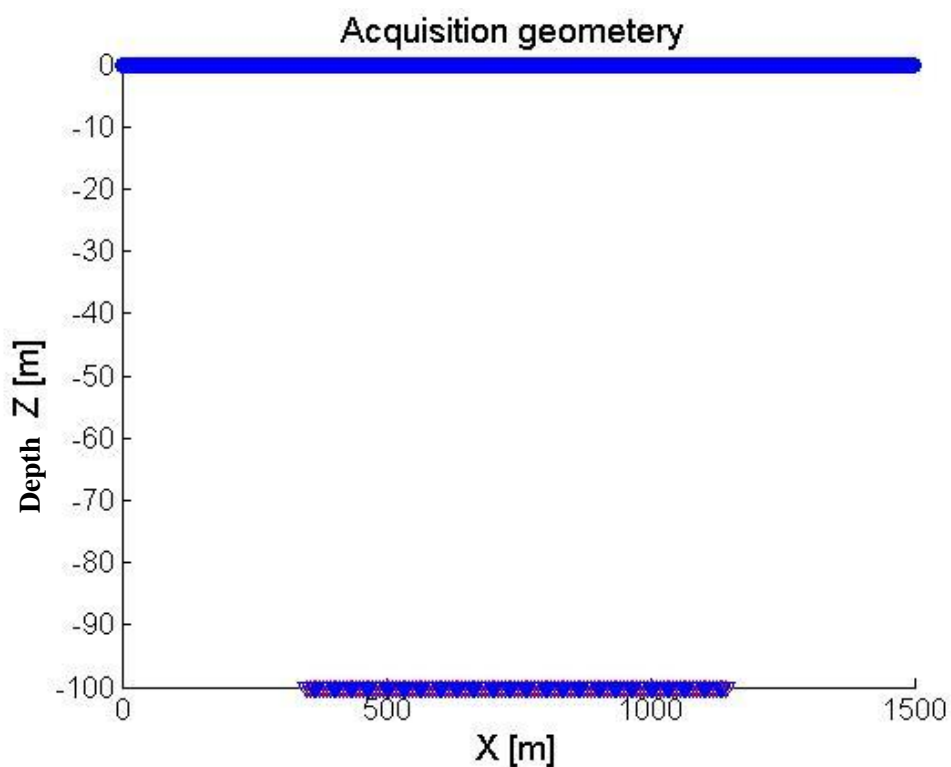
Figure 5.12: The acquisition geometry, sources are indicated with red color and receivers with blue color along the streamer (the sea-surface indicated in zero level and receivers and sources in 100m depth with negative sign).
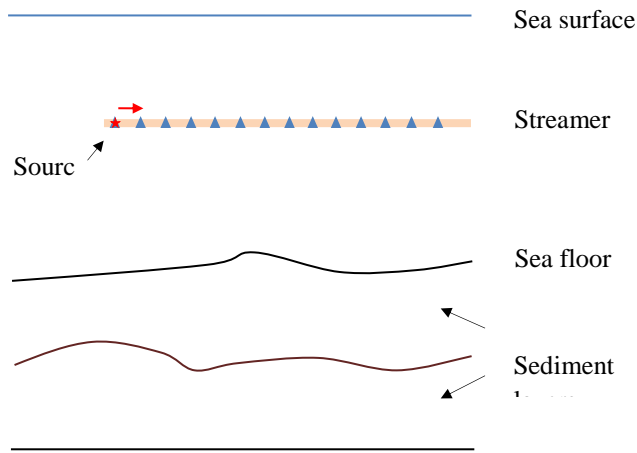
Figure 5.13: A schema of the streamer and the source, which moves over the receivers' position in a marine seismic survey with flat sea surface.
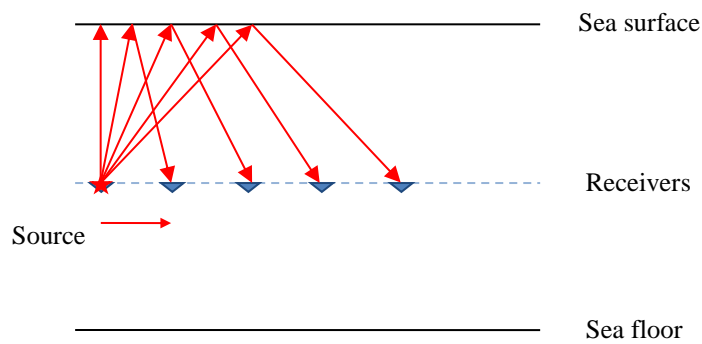

Figure 5.14: A sketch of the ray paths from a source located on the first receiver position to the sea-surface and the reflected rays from the sea-surface to the receivers on the streamer.
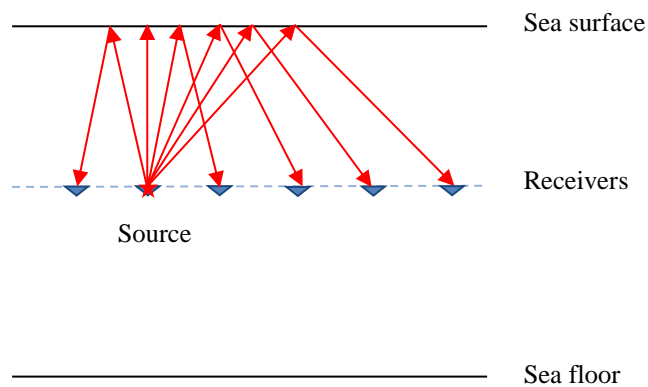

Figure 5.15: A sketch of the ray paths from a source on the second receiver position to the sea-surface and the reflected rays from the sea-surface to the receivers on the streamer.

5.4 Down-going Wavefield Computation

The integral Eq. (4.2.6) from Chapter 4 is used to compute the down-going pressure wavefield. According to this equation, for computing the down-going pressure wavefield, the flat sea-surface reflectivity was computed by using Helmholtz-Kirchhoff integral method and the up-going vertical particle velocity wavefield was computed as subsurface modelling from Nucleus+. The plot of the computed down-going wavefield by using this integral equation can be seen in Figure 5.16. There are also some edge effects in this plot that has been indicated by arrows. The integral relationship between up-going velocity and down-going pressure requires an infinite aperture measurement. However, in reality we have a finite aperture. The shape edges in the finite aperture measurement acts like a "diffractor" and introduce unwanted artifact in the reconstructed down-going pressure.
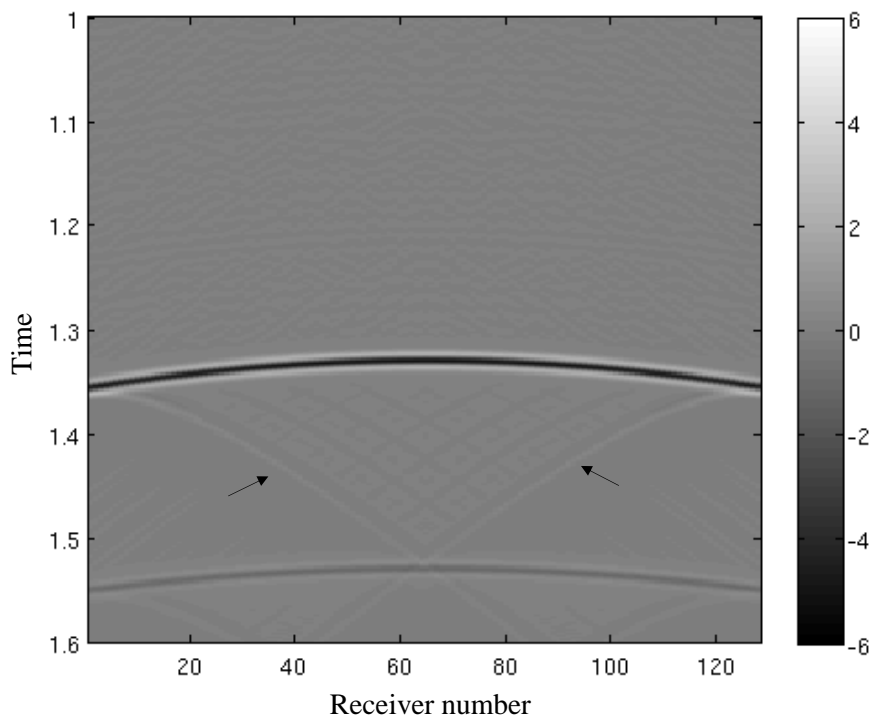

Figure 5.16: Plot of the calculated down-going wavefield, the arrows shows the edge effects.

On the other hand the total pressure wavefield (recorded by the hydrophones) was computed as subsurface modelling by Nucleus+ (see Figure 5.9).

Figure 5.17, shows the total pressure wavefield generated by Nucleus+. It consists of the up-going and down-going pressure wavefield from the first and second reflector at the sea floor in a time-receiver number plot. The reverse polarity between the up- and down-going wavefield can be clearly seen here in this plot by different gray scale colors. For better understanding the up- and

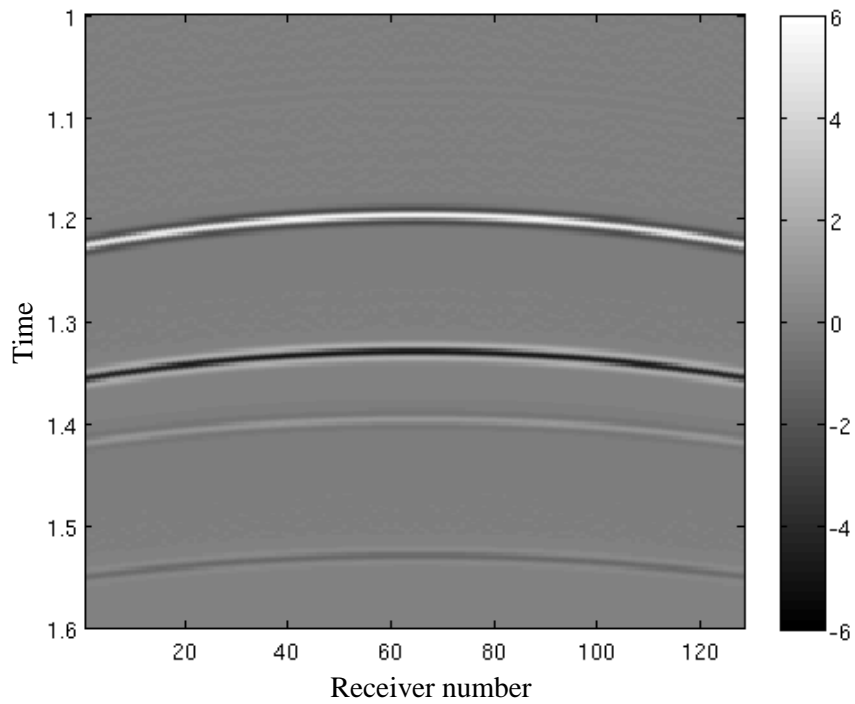down-going from the first and second reflector are separated in two Figures.

Figure 5.17: Plot of the total pressure wavefield from Nucleus+, the up-going and down-going pressure wavefield from the first and second reflector can be seen in this plot.

Figure 5.18 shows only the up- and down-going pressure from the first reflector at a depth of 1000 m (sea floor) and Figure 5.19 shows only the up- and down-going pressure from the second reflector (geological reflector) at a depth of 1200 m retrieved from Figure 5.17.
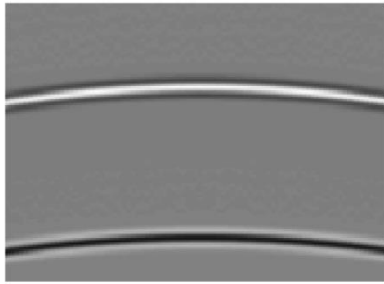
Figure 5.18: Plot of the up-going and down-going pressure from the first reflector at a depth of 1000 m (sea floor). The reverse polarity between up- and down-going pressure wavefields can be clearly seen here in this figure with different gray scale.

Figure 5.19: Plot of the up-going and down-going pressure from the second reflector at a depth of 1200 m (geological reflector). The reverse polarity between up- and down-going pressure wavefields can be seen here also in this figure with different gray scale.

The up-going wavefield that was also computed by the modelling software (Nucleus+) is shown in Figure 5.20. In this figure, arrows indicate the up-going pressure from the first and second reflector.
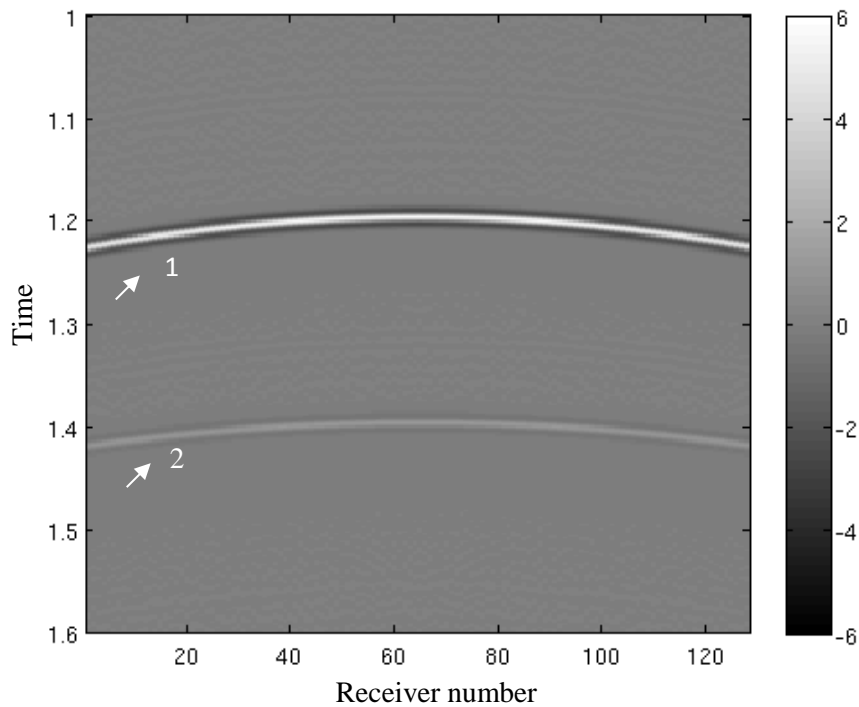

Figure 5.20 Plot of the up-going pressure wavefield from Nucleus+. Arrow no.1 shows the up-going wavefield from the first reflector and arrow no.2 shows the up-going wavefield from the second reflector.

To validate the computation of the down-going pressure wavefield in a case of flat sea-surface, the calculated down-going wavefield is subtracted from the total pressure wavefield modeled by Nucleus+. The remained data after subtraction is equivalent with the up-going pressure wavefield from Nucleus+ (see Figure 5.21). The difference shows the accuracy of the calculation.

Figure 5.21 shows the remained data after subtracting the down-going pressure wavefield from the total pressure wavefield. By comparing this plot with the modeled up-going pressure wavefield (see Figure 5.20) it can be observed that they are almost matched with each other, the only difference that can be seen in this plot is the edge effects.
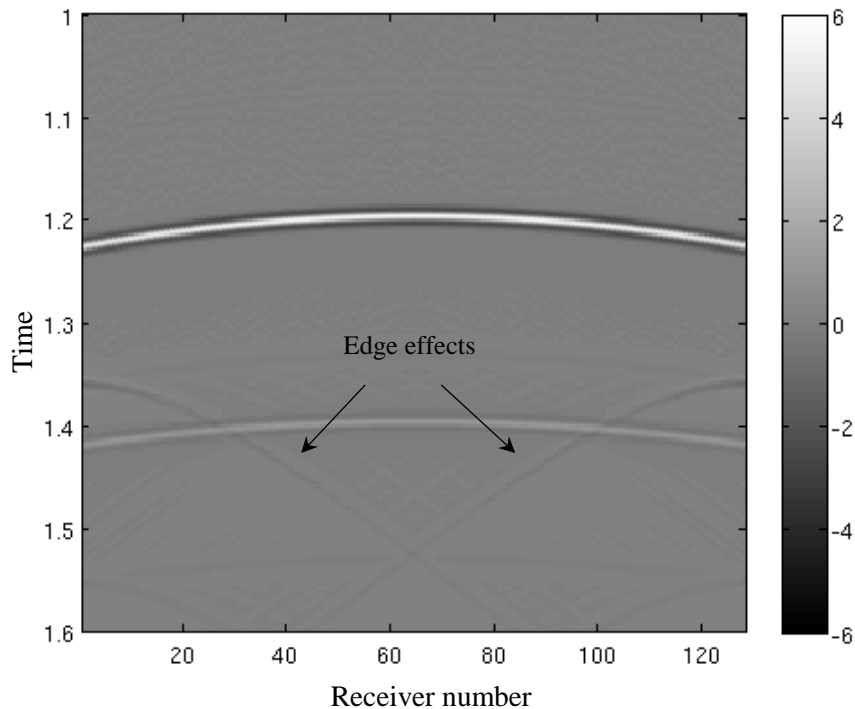

Figure 5.21: Plot of the calculated up-going wavefield by subtracting computed down-going pressure from the modeled total pressure wavefield. The edge effects have shown by arrows.

The difference between the computed up-going wavefield and the modeled up-going pressure field by Nucleus+ can be seen in Figure 5.22.
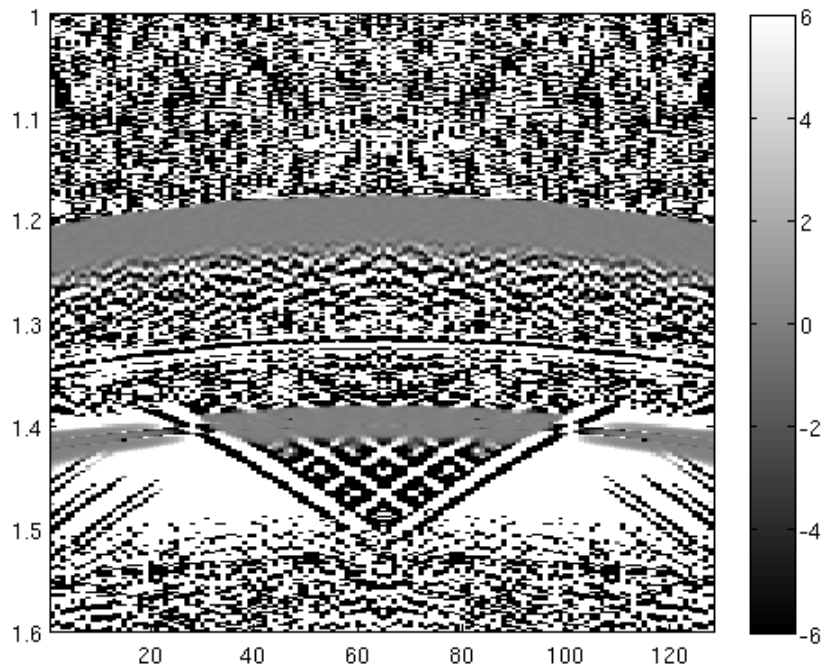
Figure 5.22: Plot shows the up-going wavefields' calculation error.

The calculation error here arises due to the edge effects which are because of the finite aperture in the down-going pressure wavefield computation. By reducing the edge effects the computed down-going pressure wavefield will be completely similar with the modeled down-going pressure wavefield.

The total pressure wavefield can be computed by adding the calculated down-going pressure wavefield including the effect of sea-surface to the modeled up-going pressure wavefield from Nucleus+. The computation accuracy of the derived down-going pressure wavefield is proved by comparing with the total pressure field from Nucleus+ using smooth and flat sea-surfaces.

The edge effect can be suppressed by tapering the input data at the edges by using cosine tapered window.

5.5 Tapering Effect

One way to remove the edge effects is tapering. For tapering, the cosine-tapered window is applied with different ratios: 0.25, 0.50 and 0.75 to the sea-surface reflectivity data modeled based on Helmholtz-Kirchhoff integral technique (Orji et al., 2011) and the up-going vertical velocity data generated by Nucleus+ before the down-going wavefield computation. This means, first

the cosine tapered window is separately applied to the sea-surface reflectivity data and the up-going vertical velocity data then by using the integral Eq. (4.2.6) obtained in Chapter 4 the down-going wavefield is computed.

In the following plots the result of using tapered window with different ratios are displayed.

Tapering with 0.25, 0.50 and 0.75 ratios

For the beginning the tapered window is applied with 0.25 ratio. Figure 5.23 shows the computed down-going pressure wavefield plot after using tapering. As it can be seen in this plot in comparison with the plot 5.16 here the edge effect has been removed completely, and this is what we expected to see after tapering.

The up-going pressure wavefield is computed in the same way as before by subtracting the computed down-going pressure wavefield after tapering from the modelled total pressure wavefield (modelled by Nucleus+). Figure 5.24 shows the up-going pressure wavefield plot. By comparing this plot with the up-going pressure wavefield plot from Figure 5.21, it can be understood that there is no edge effects in this plot after using the cosine-tapered window. The only problem with this plot is the remained energy from the down-going wavefield at the edges that has indicated by the arrows in the plot (see Figure 5.24). Therefore the tapering with ratio 0.25 did not worked perfectly for removing the edge effects.
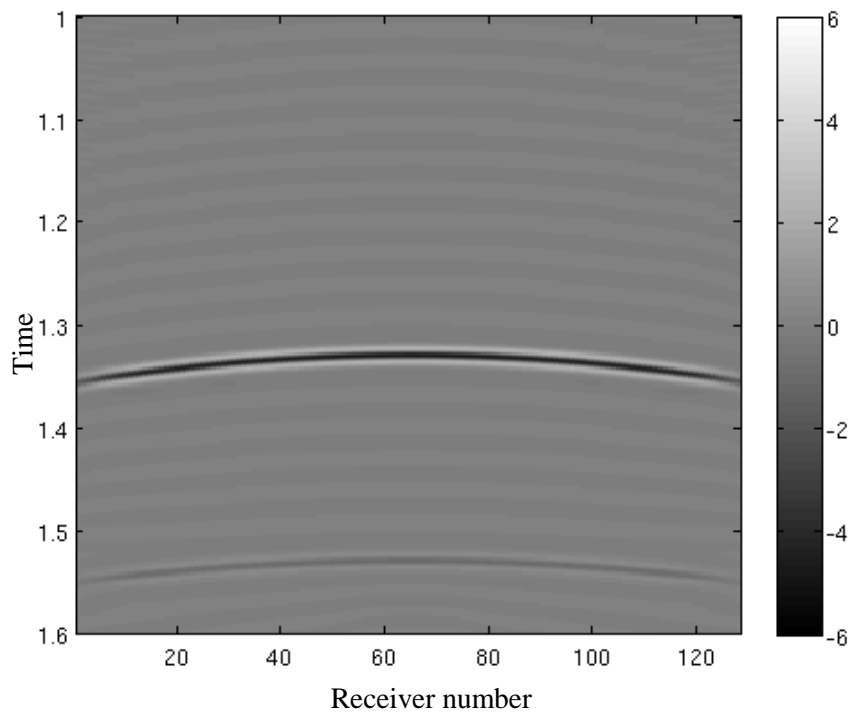
Figure 5.23: Plot of the calculated down-going wavefield after tapering with 0.25 ratio.
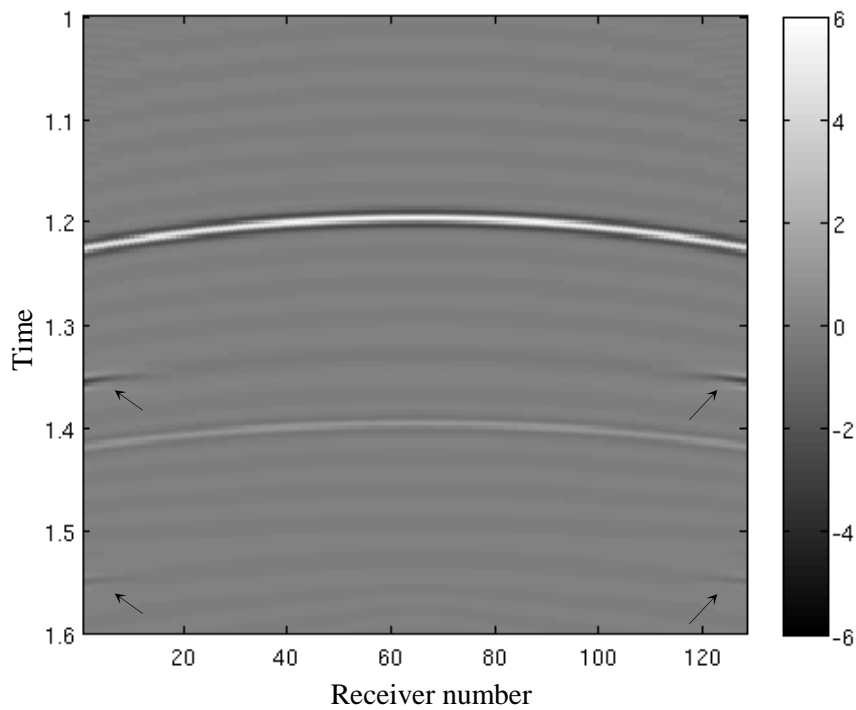

Figure 5.24: Plot of the calculated up-going wavefield (total pressure wavefield from Nucleus+ minus the calculated down-going pressure) after tapering with 0.25 ratio. The remained energy from the down-going pressure wavefield is shown by arrows.

In the next stage, the tapering process is repeated with a cosine tapered window with the ratio 0.50 to check if it works better with greater ratio than before. Figure 5.25 shows that the edge effects have been removed from the down-going pressure wavefields plot.

Figure 5.26 shows the up-going wavefield plot. There are no edge effects in this plot but as it can be seen in this figure the remained power from the down-going pressure wavefield is greater than the last case by the cosine tapered window with 0.25 ratio. So again here because of the remained power at the edges tapering with the ratio 0.50 doesn't help for removing the edge effects.
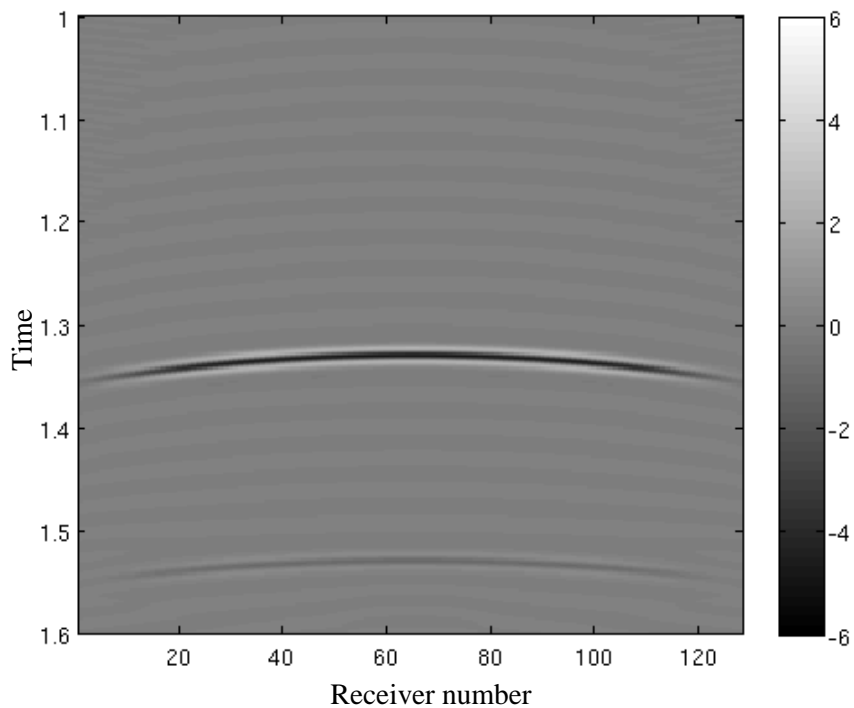

Figure 5.25: Plot of the calculated down-going wavefield after tapering with 0.50 ratio.
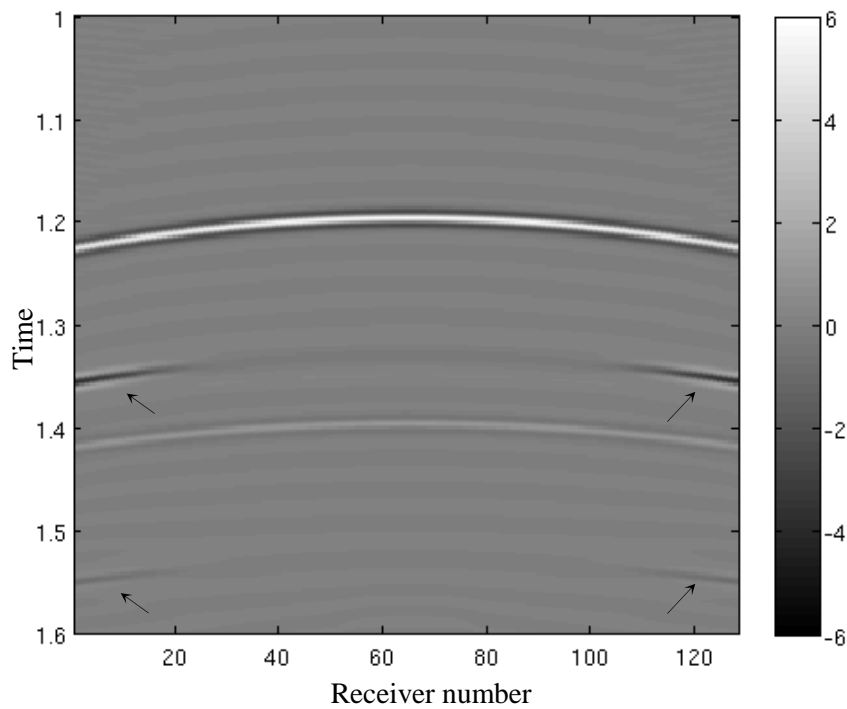
Figure 5.26: Plot of the calculated up-going wavefield (total pressure wavefield from Nucleus+ minus the calculated down-going pressure) after tapering with 0.50 ratio. The remained energy from the down-going pressure wavefield is shown by the arrows.

For the last time the tapering process is repeated with a cosine tapered window with the 0.75 ratio.

The down-going pressure wavefield is shown in Figure 5.27 after applying the tapering with the 0.75 ratio. There are no edge effects in this figure.

In spite of reducing the edge effects after tapering in the computed down-going wavefield, by increasing the tapering ratio the power at the edges in the up-going pressure wavefield is increased. Figure 5.28 shows that the power at the edges is greater than the last two cases.

Due to arising problem with the tapering we preferred to neglect the edge effects and don't use the cosine-tapered windows.
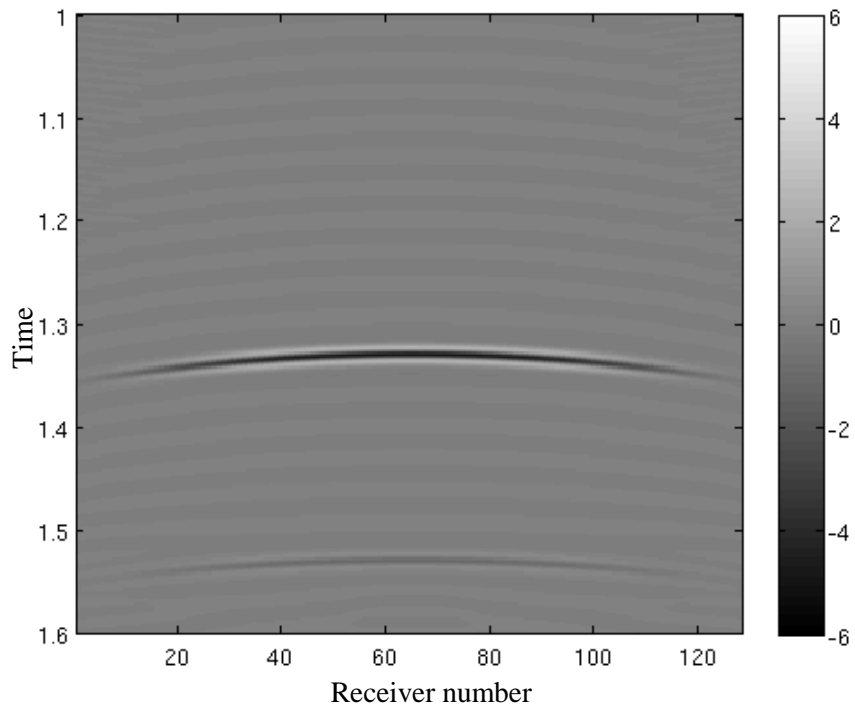
Figure 5.27: Plot of the calculated down-going wavefield after tapering with 0.75 ratio.
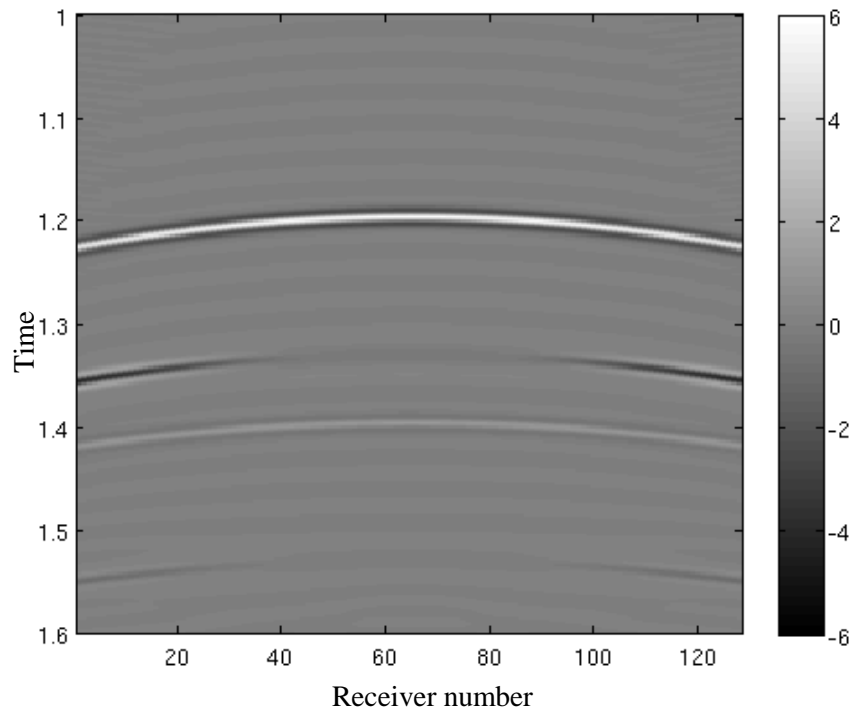

Figure 5.28: Plot of the calculated up-going wavefield (total pressure wavefield from Nucleus+ minus the calculated down-going pressure) after tapering with 0.75 ratio.

5.6 Sinusoidal Sea-Surface

Sinusoidal sea-surface is not a real sea-surface and it doesn't exist. In the case of rough sea-surface, the reflectivity from sea-surface is affected by roughness. The reflectivity and the down going wavefield are computed again for sinusoidal sea-surface as a kind of rough sea-surface. It is not possible to model sinusoidal case by Nucleus+ so we don't have the reference data to compare with the computed down-going wavefield. The sea-surface response is computed based on Helmholtz-Kirchhoff integral method (Orji et al., 2011) like the flat surface but the surface condition is replaced by sinusoidal sea-surface.

5.6.1 Modelling the Sinusoidal Sea-Surface Response

The roughness affects the propagation and scattering characteristics of a wave. The reflected wave from rough surface gets attenuated slightly due to scattering. The procedure for modelling the rough sea-surface response is the same as flat sea-surface and the only difference is that the sea-surface condition has been changed. For modelling the sea-surface response, just the same as we did for modelling the flat sea-surface the ideal seismic source which is a "spike" is considered at the same position of the receivers. Figure 5.29 shows the acquisition geometry with sinusoidal sea-surface. According to this figure the sea-surface interface is at level zero and the receivers and sources at -100 m depth level. The reflected waves from the sea-surface (down-going wavefield) referred to the response of the surface or the ghost signal. Figure 5.30 shows the sinusoidal sea-surface, streamer with the receivers and the source at the position of the first receiver and the seismic reflector at the subsurface. In this case also for modelling the sinusoidal sea-surface response, the spike source will move forward to the position of all the receivers. For each source the response is calculated for all the receivers (128 receivers).
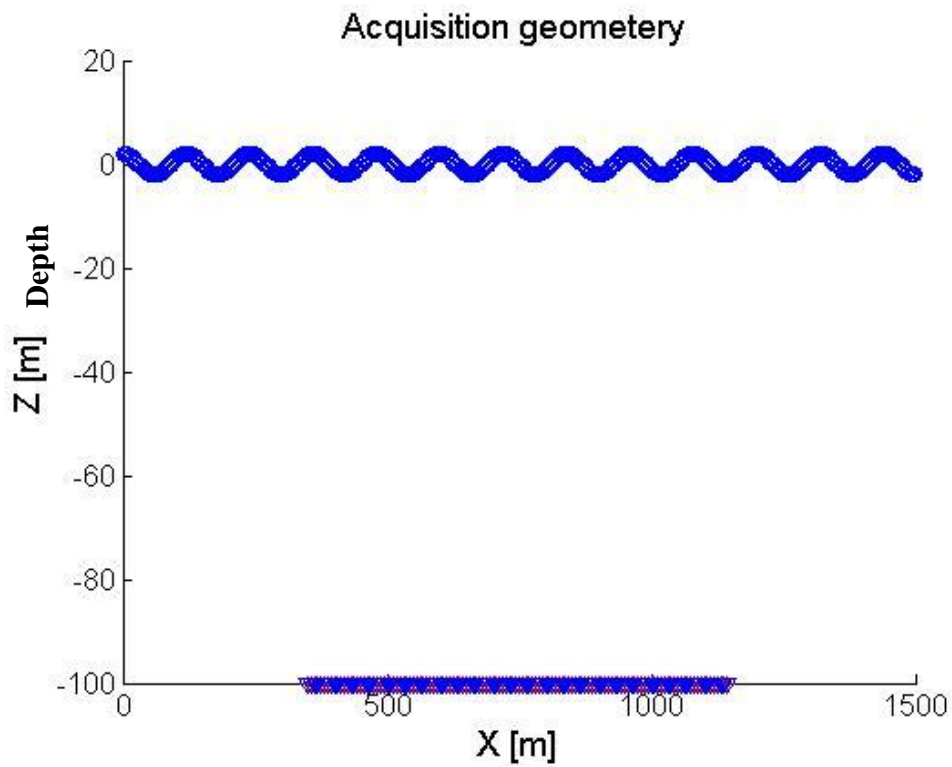
Figure 5.29: The acquisition geometry, in the plot above sources are indicated with red color and receivers with blue color.
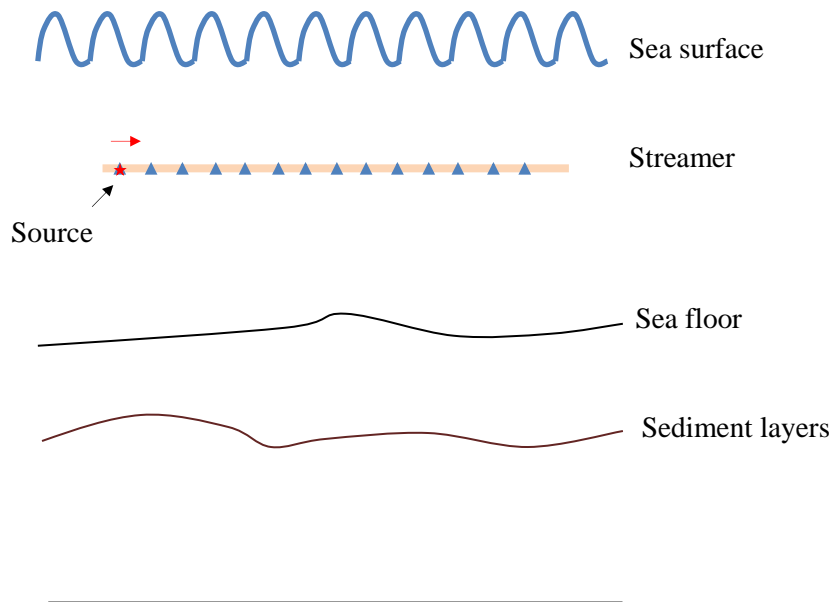

Figure 5.30: A schema of the streamer and the source which moves over the receivers' position in a marine seismic data acquisition with rough sea-surface. The red arrow shows the direction of moving the source.

5.6.2 Down-going Wavefield Computation

The integral relationship between the up-going vertical particle velocity, reflectivity of the sea-surface and the down-going pressure (Eq. (4.2.6) from Chapter 4) is used for computing the down-going pressure.

Figure 5.31 shows the reconstructed down-going pressure in a time-receiver number plot. As mentioned for flat sea-surface, there are also edge effects here due to using the finite aperture in computation. In this case some other artifacts can be seen in the plot 5.31. These are due to the shape of the sea-surface (sinusoidal) which acts like diffractors.
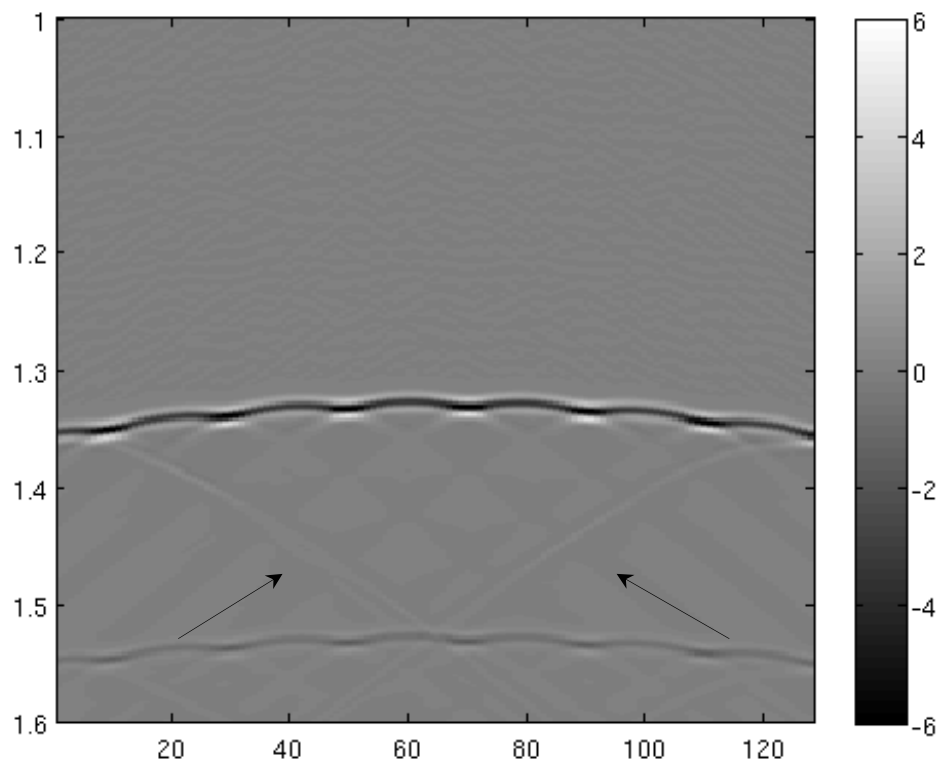

Figure 5.31: Plot of the calculated down-going wavefield for rough sea-surface. The edge effects due to the finite aperture are shown by the arrows but in this plot there are some unwanted artifacts due to sinusoidal shape of the sea-surface.

The sea-surface is flat for the data modeled by Nucleus+. Therefore, for the rough sea-surface case it is not possible to compare the result with the data generated from Nucleus+ but the computation accuracy of the derived down-going pressure was proved in the case of flat sea-surface. The only problem is the edge effects.

5.7 Rough Sea-Surface based on Pierson-Moskowitz (PM) Spectral Model

Pierson-Moskowitz sea-surface is a more realistic sea-surface. Pierson and Moskowitz supposed that if the wind blows constantly over a large area for a long time, the waves constructed by the wind will reach a balance point with the wind. This state is known as a fully developed sea. The sea-surface reflectivity is computed based on Helmholtz-Kirchhoff integral using a rough sea-surface based on Pierson-Moskowitz (PM) spectral model.

5.7.1 Modelling the Rough (PM) Sea-Surface Response

For modelling the sea-surface based on PM spectrum a point diffractor is considered at a depth level 500m at the middle below the receivers. In this case there are 500 receivers at a group interval 3m and the depth level 15m above the source. The sea-surface response is modelled like the flat and sinusoidal surface.

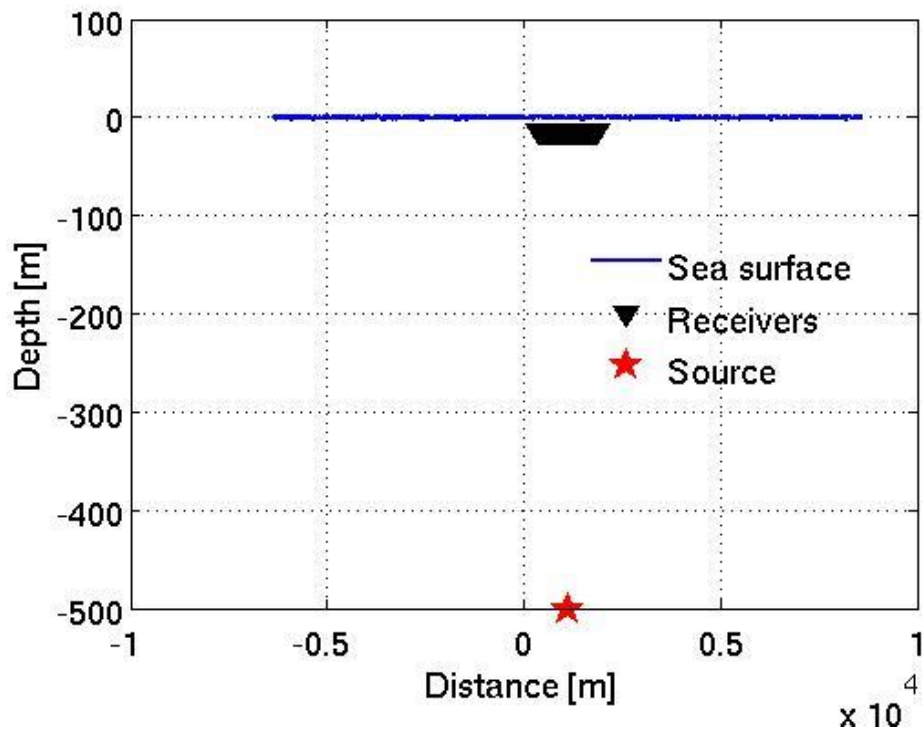Figure 5.32 shows the acquisition geometry for modelling the sea-surface by PM spectrum.

Figure 5.32: The acquisition geometry, in the plot above receivers are indicated with blue color and source with red color.

Figure 5.32 shows the table of source and receiver parameters for modelling based on PM spectrum.

Dataset : PM

Sample interval (ms) : 2.0
Recording length (ms) : 1000

Number of sources   : 1
Source depth (m)   : 500.0

Number of streamers : 1
Streamer type   : Geostreamer
Streamer depth (m) : 15.0
No. groups/streamer : 500
Group interval (m) : 3.0

Positions of sources :

Number   X   Y
   1   1098.5   0.00

Position of first receiver on streamer :

Number   X   Y
   1   350.0   0.00

Figure 5.33: Table of the vessel parameter for modelling the sea-surface based on PM spectrum.

The modeled sea-surface based on Pierson-Moskowitz with the wind speed $10 \, {}^m/_s$ is shown in Figure 5.34 (The wave height is estimated by sea-surface function (3.3) from Chapter 3). This figure shows the more realistic rough sea-surface.
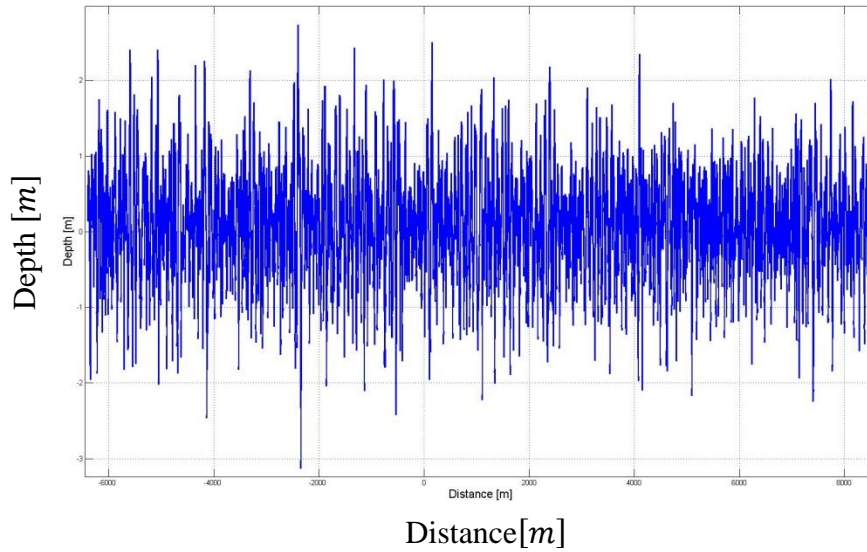
Distance[m]

Figure 5.34: The sea-surface spectrum estimated by the PM sea-surface function with the $10\,{}^m/_s$ wind speed.

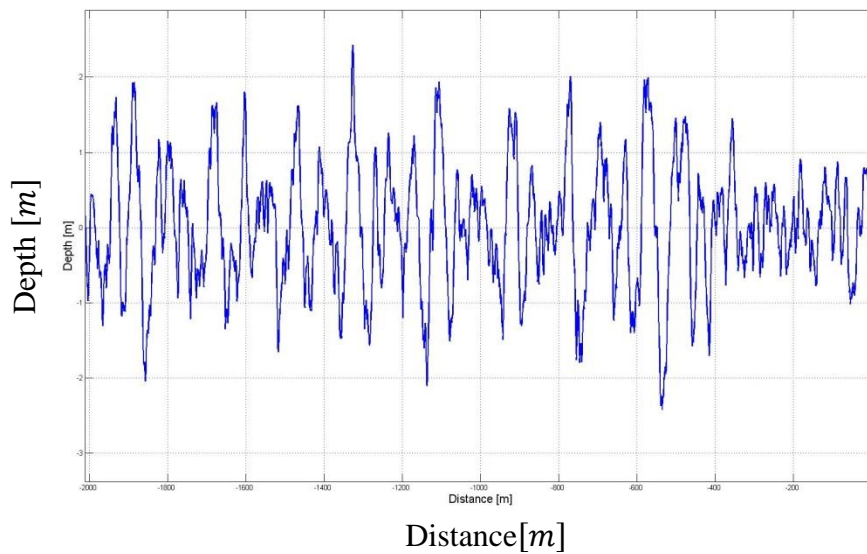A larger scale of Figure 5.34 can be seen in Figure 5.35.

Distance[m]

Figure 5.35: A larger scale of the sea-surface spectrum estimated by the PM sea-surface function with the $10\,{}^m/_s$ wind speed.

Figure 5.36 shows the sea-surface with the wind speed $15\,{}^m/_s$. In comparison with Figure 5.34, it can be seen clearly that the sea waves are larger in Figure 5.36. The difference in the sea-surface function in this case is the wind speed which is higher than the last one.
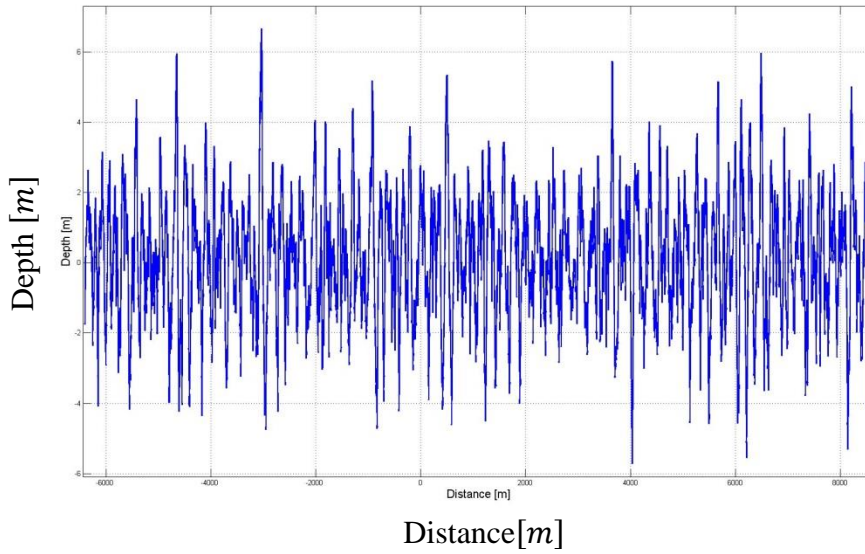
Distance[m]

Figure 5.36: The sea-surface spectrum estimated by the PM sea-surface function with the $15\,{}^{m}\!/_{s}$ wind speed.

For better perception Figure 5.37 shows a larger scale of Figure 5.36.
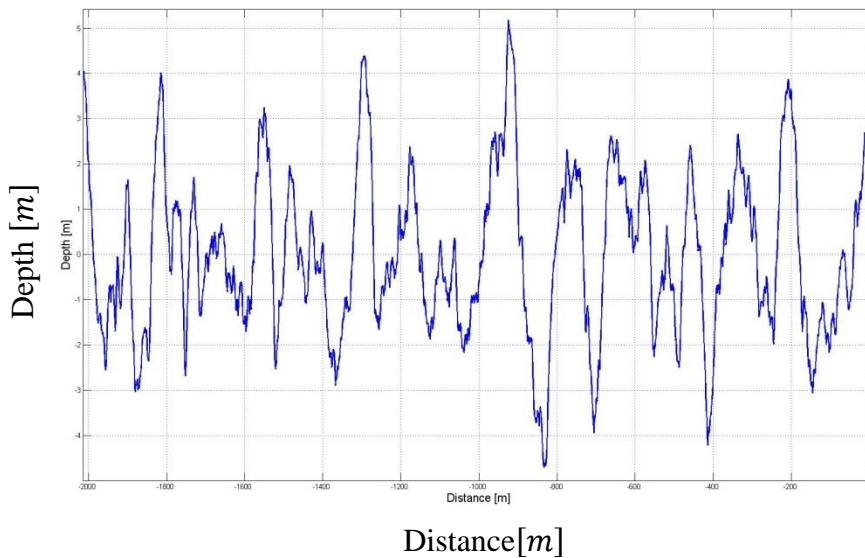

Distance[m]

Figure 5.37: A larger scale of the sea-surface spectrum estimated by the PM sea-surface function with the $15\,{}^{m}\!/_{s}$ wind speed.

Figure 5.38 shows the generated waves with the wind velocity $20\,{}^{m}\!/_{s}$. The wave height in this case is more than the wave generated by the wind velocity $10\,{}^{m}\!/_{s}$, $15\,{}^{m}\!/_{s}$. Therefore as the wind gets more power and higher velocity, the wave gets bigger.

Eventually, the waves are going to interact with each other to generate longer waves (Hasselmann et al., 1973). The interaction leads the wave energy from shorter wave to the higher frequencies just below the peak of the wave spectral density (see Figure 5.40). Finally as declared by Pierson and Moskowitz waves goes faster than the wind.
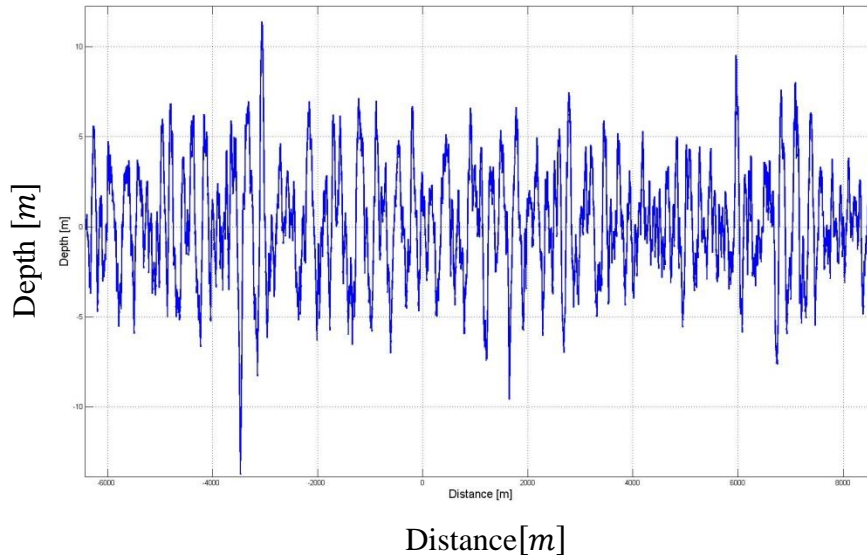

Figure 5.38: The sea surface spectrum estimated by the PM sea surface function with the $20 \, {}^m/_s$ wind speed.
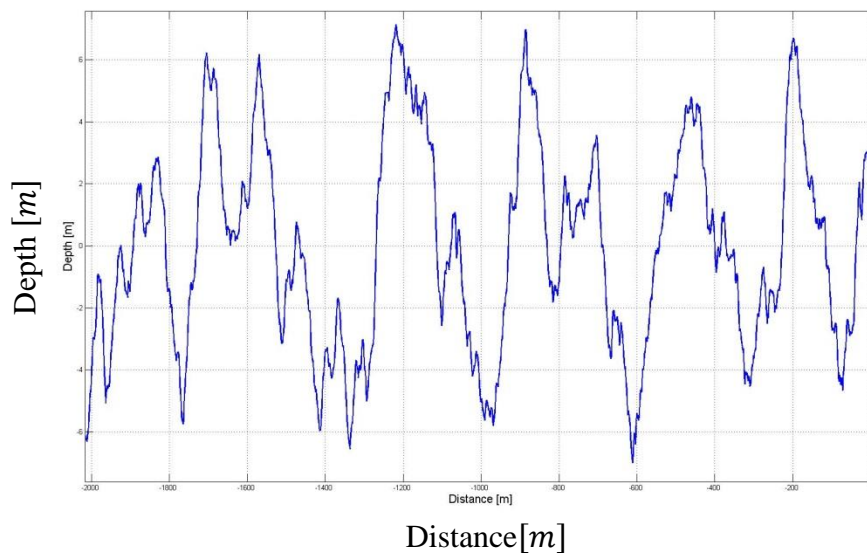

Figure 5.39: The sea-surface spectrum estimated by the PM sea-surface function with the $20 \, {}^m/_s$ wind speed.

Figure 5.39 shows a larger scale of the generated waves with the wind velocity $20\ ^m/_s$.
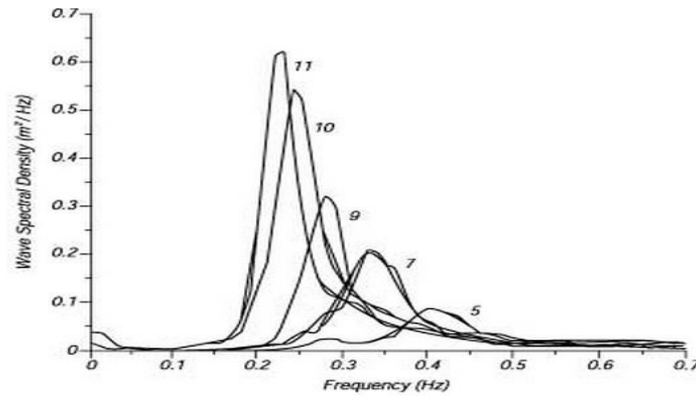

Figure 5.40: Wave spectral density of a developed sea for different fetches (picture from Hasselmann st al., 1973)

5.7.2 Down-going Wavefield Computation

Eq. (4.2.6) from Chapter 4 is used again to compute the down-going pressure wavefield. For modelling the sea-surface, the Eq. (3.3) from chapter 3 is used but the sea-surface reflectivity is computed based on Helmholtz-Kirchhoff integral method (Orji et al., 2011).

The following figures show the computed down-going wavefield based on Pierson-Moskowitz spectral model.

Figure 5.41 shows the computed down-going pressure wavefield using a more realistic rough sea-surface based on Pierson-Moskowitz spectrum. based on Pierson-Moskowits spectral model in a time-receiver (channel nr.) plot. For better perception a zoomed format of this plot can be seen in the Figure 5.42. The unwanted artifacts due to the roughness of the surface can be seen in these figures.
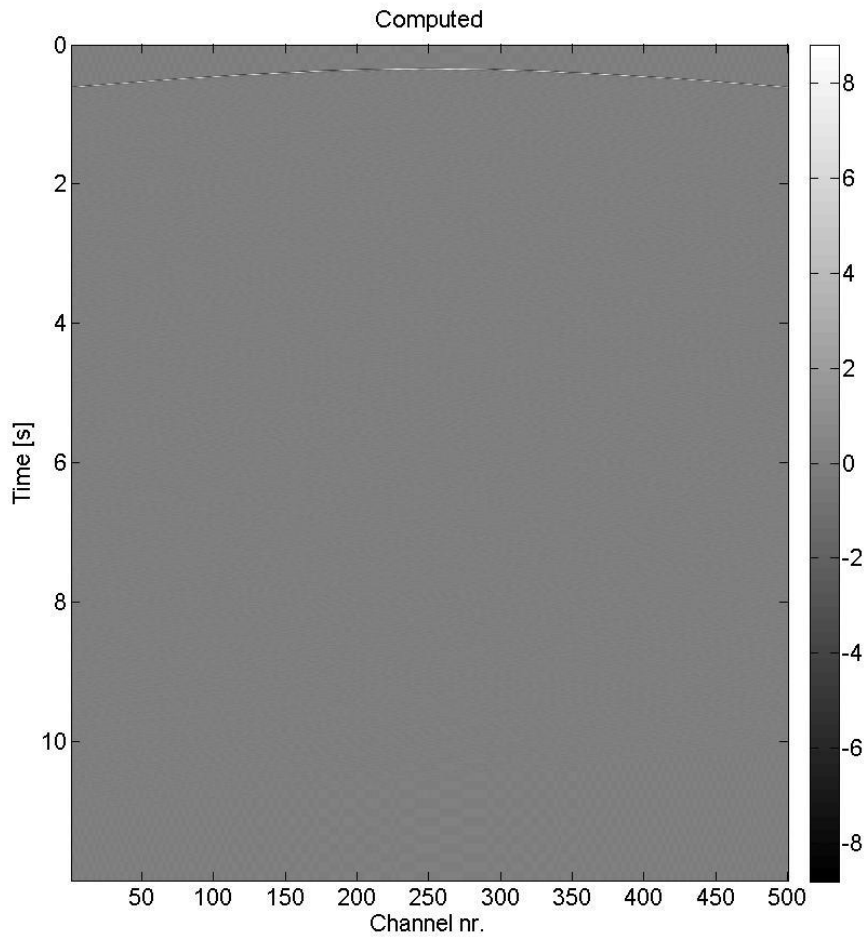
Figure 5.41: The reconstructed down-going pressure wavefield based on Pierson-Moskowitz spectral model in a time-channel nr. plot.

In this case, there is no reference data to compare with the computed down-going wavefield neither.
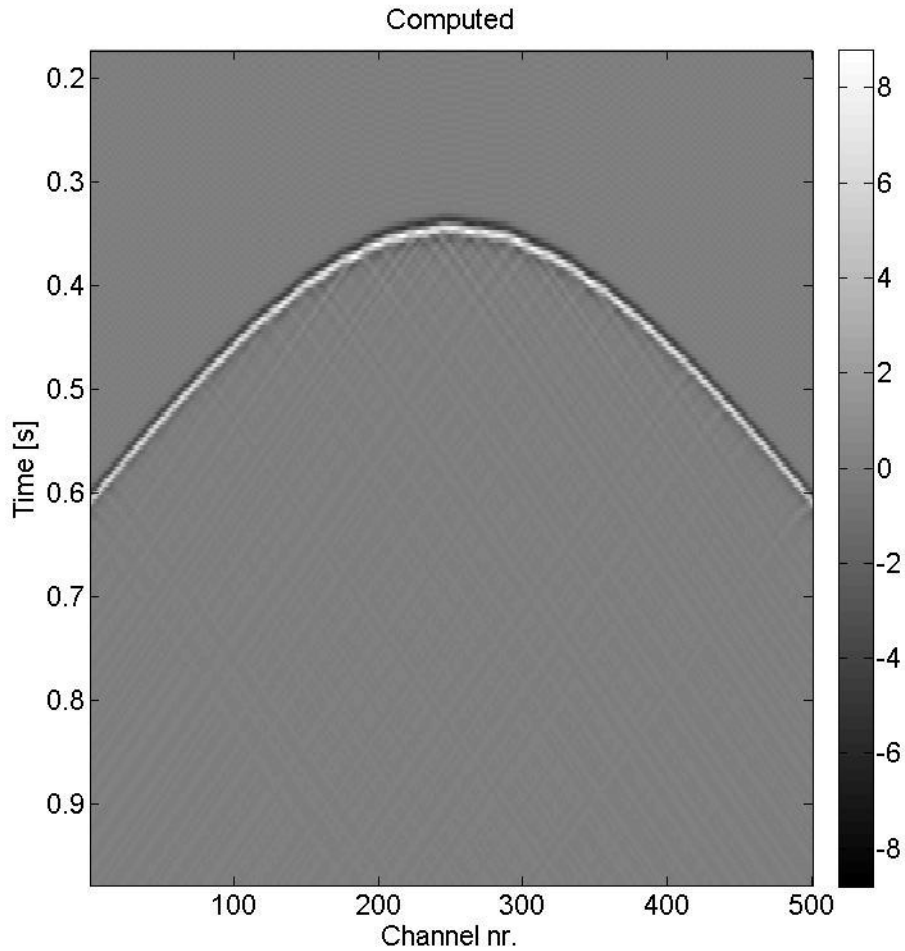
Figure 5.41: A zoomed format plot of the reconstructed down-going pressure wavefield based on Pierson-Moskowitz spectra in a time-channel nr. plot.

The integral relation derived from Rayleigh's reciprocity theorem was used for computing the down-going pressure wavefield from the up-going velocity wavefield and the sea-surface reflectivity. The up-going vertical particle velocity was modelled by Nucleus+ and the sea-surface response was computed based on Helmholtz-Kirchhoff integral using a free-surface boundary. The down-going wavefield computation accuracy was proved by comparing with the total pressure wavefield from Nucleus+ using flat sea-surface. The modelling was tested on sinusoidal and on a more realistic rough sea-surface based on Pierson-Moskowitz (PM) spectrum.

Chapter 6

Conclusion & Future Work

6.1 Conclusion

Ray tracing is a widely used method for modelling seismic wave propagation. Nucleus+, the PGS proprietary software, has a ray tracing tool that allows users to model seismic wave propagation. However, ray tracing technique has an inherent limitation for modelling seismic data from a highly varying medium. As a consequence, seismic data from a spatio-temporally varying rough sea-surface cannot be obtained using ray tracing technique.

In this thesis, an integral relationship is formulated that links the up-going vertical particle velocity to that of the down-going pressure wavefield. The up-going wavefield can be modelled using ray-tracing technique (e.g. using Nucles+). Using this modelled up-going wavefield, the down-going pressure wavefield from rough sea surfaces are reconstructed. The validity of the integral relationship for the reconstruction of the down-going pressure wavefield is demonstrated using a flat, sinusoidal and a more realistic rough sea-surface (based on Pierson-Moskowitz spectrum). For the flat sea-surface case, the reconstructed down-going pressure wavefield is quantitatively compared with that of a modeled reference and a reasonably small error is obtained. For the case of rough sea-surface, a successful reconstruction of the down-going pressure wavefield was demonstrated.

6.2 Future Work

This work was done by using a 2-D marine seismic acquisition model which acquires data from single streamer. The same analysis should be performed on data generated using 3-D seismic survey which involves many streamers with multiple arrays of airguns towed by the vessel. The study could also be expanded to consider more realistic earth model for data modelling.

It is also recommended to perform the same analysis on modeled data based on the Finite difference method by Nucleus+.

Bibliography

Amundsen, L., 1993, *Wavenumber-based filtering of marine point-source data*: Geophysics, **58**, No.9, 1335-1348.

Amundsen, L., 2001, *Elimination of free-surface related multiples without need of the source wavelet*: Geophysics, **66**, 327-341.

Amundsen, L., Røsten, J. O. A. Robertsson, and E. Kragh, 2005, *Rough-sea deghosting of streamer seismic data using pressure gradient approximations*: Geophysics, **70**, V1-V9.

Baldock, S., H. Masoomzadeh, N. Woodburn, A. Hardwick, and T. Travis, 2013, *Increasing the bandwidthof marine seismic data*: PESA News Resources.

Berni, A., 1985, *Marine seismic system*, United State patent, no. 4,520,467.

Carlson, D., A. Long, W. Söllner, H. Tabti, R. Tenghamn, and N. Lunde, 2007, *Increased resolution and penetration from a towed dual-sensor streamer*: First Break, **25**, 71-77.

Gelius, L. J., 2007, *Introduction to seismic processing and imaging*: GeoClass, Chapter 2, 2.3.

Ghosh, S. K., 2000, *Deconvolving the ghost effect of the water surface in marine seismics*: Geophysics, **65**, 1831-1836.

Hajnsek, L., K. Papathanassiou, 2005, *Rough Surface Scattering Models.*

Hansen, R. E., 2013, *Imaging, Introduction to Sonar*: Department of Informatics, University of Oslo.

Hasselmann, K., et al., 1973, *Measurements of wind- wave growth and swell decay during the joint North Sea Wave Project (JONSWAP)*, 8, 12, 7-95.

Hasselmann, D. E., M. Dunckel and J. A., Ewing, 1980, *Directional wave spectra observed during JONSWAP 1973*, J. Phy. Oc. **10**, 1264-1280.

Hasselmann, S., K. Hasselmann and G. J. Komen, 1984, *On the existence of a fully developed wind sea spectrum:* J. Phys. Oceanogr. **14**, 1271-1285.

Ishimaru, A., 1999, *Wave Propagation and Scattering in Random media*, Chapter 21.

Miles, J. W. (1957), *On the generation of surface waves by shear flows*, Journal of Fluid Mechanics 3 (2): 185–204.

Moldoveanu, N., N. Seymour, D. J. Manen and P. Caprioli, 2012, *Broadband seismic methods for towed-streamer acquisition*: 74th EAGE Conference and Exhibition incorporating SPE EUROPEC 2012.

Orji, O. C., W. Söllner, and L. J. Gelius, 2010, *Imaging the sea surface using a dual- sensor towed streamer*: Geophysics, **75**, V111-V118.

Orji, O. C., W. Söllner, and L. J. Gelius, 2011, *Imaging time varying sea surface using dual- sensor data.*

Ozbek, A., M. Vassallo, K. Ozdemir, D. J. Van Manen, and K. Eggenberger, 2010, *Crossline wavefield reconstruction from multi component streamer data*: Part 2 – *Joint interpolation and 3D up/down separation by generalized matching pursuit*: Geophysics, **75**, WB69-WB85.

Ray,C., 1982, *High resolution marine stratigraphic system,*United States patent, no. 4, 353,121.

Robertsson, J. O. A., R. Laws, Ch. Chapman, J. P. Vilotte and E. Delavaud, 2006, *Modelling of scattering of seismic waves from a corrugated rough sea surface: a comparison of three methods*: : Geophysics, **167**, 70-76.

Robertsson, J. O. A., I. Moore, M. Vassallo, A. K. Ozdemir, D. J. Van Manen, and A. Ozbek, 2008, *On the use of multicomponent streamer recordings for reconstruction of pressure wavefields in the crossline direction*: Geophysics, **73**, A45-A49.

Semb, P., H., Fromyr, E., Caselitz, B., Lie, O., 2010, *Comparison of deep tow conventional hydrophone and dual sensor streamer seismic offshore Egypt*, 80th SEG Annual International Meeting, Expanded Abstracts, **29**, 16-20.

Söllner, W., and S. Hegna, 2011, *Method for separating up and down propagating pressure and vertical velocity fields from pressure and three-axial motion sensors in towed streamers*, Justia Patents Database, App. No. 20110242937.

Sonneland, L., L. Berg, P. Eidsvig, A. Haugen, B. Fotland, I. Vestby, 1986, *2D deghosting using vertical receiver arrays*, 56th SEG Annual International Meeting, Expanded Abstracts, **5**, 516-519.

Stephen, R. A., 1996, *Modelling sea surface scattering by the time-domain finite-difference method*, Acoustical Society of America.

Sun, Y., R. G. Clapp, and B. Biondi, 1997, Three *dimensional dynamic ray tracing in complex geological structures,* Stanford Exploration Project, **93**, 63-75.

UniGEO 2013, *GeoCLASS.* From http://www.unigeo.no/home/page.php?9.

Whitmore, N. D., A. A. Valenciano, W. Söllner, and Sh. Lu, 2010, *Imaging of primaries and multiples using a dual-sensor streamer*, SEG Denver 2010 Annual Meeting.

Wu, R. S., V. Maupin, P. Moczo, J. O. A. Robertsson, and L. Eisner, 2007, Advances in wave propagation in heterogeneous earth, *The finite-difference time-domain method for modelling of seismic wave propagation*: Geophysics, **48**, 421-516.

Ziolkowski, A., 1970, *A method for calculating the output pressure waveform from an air gun,* Geophys. J. R. Astr. Soc. 21, 137-161.

Related background acknowledgements

Amundsen, L., 1993, *Wavenumber-based filtering of marine point-source data*: Geophysics, **58**, No.9, 1335-1348.

Amundsen, L., 1994, *The propagation matrix related to the Kirchhoff-Helmholtz integral in inverse wavefield extrapolation*: Geophysics, **59**, No.11, 1902-1910.

Born, M., E. Wolf, and A. B. Bhatia, 1999, *Principles of optics*, *Kirchhoff's diffraction theory*, Cambridge University Press, Chapter 8, 418-425.

Frijilink, M., R. V. Borselen, and W. Söllner, 2011, *The free surface assumption for marine seismic data-driven demultiple methods*: Geophysical Prospecting, **59**, 269-278.

Gelius, L. J. and T. A. Johansen, 2012, *Petroleum Geophysics*, VOL II, UNIGEO.

Musil, M., and C. Kostov, 2008, *A 2.5D method for removal of free-surface related seismic events*: 70th EAGE Conference and Exhibition.

Orji, O. C., W. Söllner, and L. J. Gelius, 2012, *Effects of time-varying sea surface in marine seismic data*: Geophysics, **77**, 33-43.

Shah, P. M., 1973, *Ray tracing in three dimensions*: Geophysics, **38**, No.3, 600-604.

Shearer, P. M., 2009, *Introduction to seismology*, *Kirchhoff Theory*, Cambridge University Press, Chapter 7, 180-190.

Siderius, M., and M. B. Porter, 2008, *Modeling broadband ocean acoustic transmissions with time-varying sea surface*: Acoustical Society of America,137-150.

Söllner, W., E. Brox, M. Widmaier, and S. Vaage, 2008, *Surface related multiple suppression in dual-sensor towed streamer data*: 70th EAGE Conference and Exhibition.

Wapenaar, K., E. Slob, and R. Snieder, 2008, *Seismic and electromagnetic controlled-source interferometry in dissipative media*: Geophysical Prospecting, **56**, 419-434.